Solid State Nuclear Magnetic Resonance, 1 (1992) 267–295
Elsevier Science Publishers B.V., Amsterdam

Sidebands in dynamic angle spinning (DAS) and double rotation (DOR) NMR

B.Q. Sun, J.H. Baltisberger, Y. Wu, A. Samoson and A. Pines

Materials and Chemical Sciences Division, Lawrence Berkeley Laboratory, 1 Cyclotron Road, and Chemistry Department, University of California, Berkeley, CA 94720, USA

(Received 25 September 1992; accepted 4 October 1992)

Abstract

A theory of dynamic angle spinning (DAS) and double rotation (DOR) NMR is described using average Hamiltonian and irreducible tensor methods. Sideband intensities in DAS and DOR spectra are analyzed by both the moment and Bessel function methods, and general formulae are derived. Results show that the DAS moments depend on the relative rotor phase between the first and the second evolution periods, whereas the second and third DOR moments are independent of the relative phase between the inner and outer rotors. Sideband intensities in DAS spectra also depend on the relative rotor phases between evolution at the first and second angles, as well as on the ratio of time spent at each angle. Sideband intensities and phases in DOR spectra are related to the relative rotor phases between the inner and outer rotors, and the sideband pattern is determined by the ratio of the inner and outer rotor spinning speeds. An inversion symmetry of the odd numbered DOR sidebands at the relative rotor phase $\gamma_r = 0°$, 180° permits the elimination of these sidebands. Finally, numerical simulations are implemented and shown to agree with experimental results. Quadrupolar parameters can therefore be recovered either by calculating the second and third moments or by simulating the sideband intensities and phases.

Keywords: dynamic-angle spinning; double rotation; spinning sidebands; quadrupolar nuclei; central transition

Introduction

Nuclear magnetic resonance has often been used to provide information about local bonding environments for a wide range of nuclei. For nuclei with half-integer spins ($I > \frac{1}{2}$), the broadening of the central transition ($\frac{1}{2} \leftrightarrow -\frac{1}{2}$) in a polycrystalline or amorphous sample comes primarily from second-order effects involving the nuclear quadrupolar moment interacting with local electric field gradients (EFG) [1–3]. From a sample with only one site, the quadrupolar coupling and chemical shift information may be obtained through analysis of the powder pattern. When many inequivalent sites are present in a sample, however, this analysis is complicated by overlapping features which are hard to deconvolute, making the application of solid state NMR difficult for a large class of nuclei. The technique of magic-angle spinning (MAS) [4,5] has been successful for improving the resolution of nuclear signals that are broadened by either the chemical shift anisotropy (CSA) or dipole–dipole interactions, both of which have a spatial dependence proportional to a second-rank tensor. For most quadrupolar nuclei, though, MAS only reduces the linewidth of the central transitions by about a factor of three, since the anisotropy of a second-

---

Correspondence to: Professor A. Pines, Chemistry Department, University of California, Berkeley, CA 94720, USA.

0926-2040/92/$05.00

order quadrupolar interaction is determined by a linear combination of both second- and fourth-rank spatial tensors [6–10]. Further study has demonstrated that the second-order anisotropic broadening may be suppressed by making the spinning trajectories time dependent [6]. In particular, dynamic angle spinning (DAS) [7,8] as well as double rotation (DOR) [9–11] have been shown to create the correct spinning trajectories for averaging both second- and fourth-rank spatial tensors.

DAS experiments are implemented by allowing the sample to evolve at multiple angles sequentially in time, through a flipping of the spinning axis, thereby canceling both the second- and fourth-rank spatial tensors. In DOR, by contrast, a small inner rotor spins within an outer rotor. The inner rotation is about an axis tilted at $\theta^{(4)} = 30.56°$ (one of the magic angles of the fourth-order Legendre polynomial) with respect to the spinning axis of the outer rotor. The outer rotor spins about an axis inclined at $\theta^{(2)} = 54.74°$ (the magic angle of the second-order Legendre polynomial) relative to the external magnetic field. Owing to mechanical limitations, typical spinning speeds in DAS experiments are in the range of 3 to 10 kHz, while under DOR the outer rotor spins at about 1 kHz and the inner rotor at about 5 kHz. In many cases these spinning speeds are not fast enough to completely average the quadrupolar interaction, which is inhomogeneous, and spinning sidebands consequently appear in the DAS and DOR spectra. Although the presence of sidebands may make assignments difficult, they may also carry enough information to allow the extraction of the quadrupolar and chemical shift parameters [12–14].

In this paper, sideband intensities in DAS and DOR are analyzed using both the moment method proposed by Maricq and Waugh [12] and the Bessel function expansion used by Herzfeld and Berger [13] for MAS spectra. General formulae for the calculation of moments and sideband intensities are derived. Similar to the MAS case, the sideband intensities are generally dependent on the quadrupolar parameters (ω_Q and η_Q) and the sample spinning speeds. One major difference arises, however, since the sideband intensities in DAS spectra also depend on the relative rotor phases between evolution at the first and second angles, as well as on the ratio of time spent at each angle. Sideband intensities and phases in DOR spectra are related to the relative rotor phases between the inner and outer rotors, and the sideband pattern is determined by the ratio of the inner and outer rotor spinning speeds. Quadrupolar parameters can therefore be recovered by simulating the sideband intensities and phases. Numerical simulations are implemented and shown to agree with experimental results.

The first-order average Hamiltonian with a quadrupolar interaction

We consider a spin system subjected to a quadrupolar interaction in the presence of a strong, static external magnetic field. Its spin Hamiltonian in the laboratory frame is [15]

$$\mathscr{H}_{\mathrm{LAB}} = \mathscr{H}_{\mathrm{Z}} + \mathscr{H}_{\mathrm{Q}} = \omega_0 I_z + \omega_{\mathrm{Q}} \sum_{m=-2}^{2} (-1)^m A_{2-m} T_{2m} \tag{1}$$

where ω_0 is the Larmor frequency and ω_{Q} is the quadrupolar coupling constant, given by

$$\omega_Q = \frac{e^2 qQ}{2I(2I-1)\hbar} \tag{2}$$

$A_{2,m}$ and $T_{2,m}$ are the elements of the second-rank irreducible spatial and spin tensors, respectively. The spin irreducible tensor elements, $T_{2,m}$, are defined in terms of the spherical angular momentum operators (I_0, $I_{\pm}$) for the quadrupolar interaction as

$$T_{2,0} = \frac{1}{\sqrt{6}}(3I_0^2 - I^2) \tag{3a}$$

$$T_{2,\pm 1} = \mp \tfrac{1}{2}(I_0 I_{\pm} + I_{\pm} I_0) \tag{3b}$$

$$T_{2,\pm 2} = \tfrac{1}{2} I_{\pm}^2 \tag{3c}$$

The spatial irreducible tensor elements, $A_{2,m}$, can be represented by the principal values, anisotropy (δ_Q), and asymmetry parameter (η_Q) of the quadrupolar coupling tensor as

$$A_{2,m} = \sum_{m'} \mathscr{D}^{(2)}_{m',m}(\Omega)\rho_{2,m'} \tag{4}$$

where $\mathscr{D}^{(2)}_{m',m}(\Omega)$ are components of the Wigner rotation matrices, Ω are Euler angles for the transformation to the laboratory frame from the principal axis system (PAS) of the quadrupolar interaction, and

$$\rho_{2,0} = \sqrt{\tfrac{3}{2}}\,\delta_Q \tag{5a}$$

$$\rho_{2,\pm 1} = 0 \tag{5b}$$

$$\rho_{2,\pm 2} = \tfrac{1}{2}\delta_Q\eta_Q \tag{5c}$$

In our case, $\delta_Q = 1$.

The quadrupolar coupling constant appearing in eqn. (1) can be related to the electrical-field-gradient tensor (EFG), which is determined by the charge distribution around a particular nucleus in the molecule. Measurement of the quadrupolar coupling constant therefore provides a method of obtaining local bonding information. In order to extract this information, we need to know how the density matrix evolves under the quadrupolar spin Hamiltonian. Following the conventional procedure, the total spin Hamiltonian in eqn. (1) is transformed from the laboratory frame into the rotating frame (or interaction representation):

$$\begin{aligned}\mathscr{H}(t) &= e^{i\omega_0 I_z t}\mathscr{H}_Q e^{-i\omega_0 I_z t}\\ &= \omega_Q \sum_{m=-2}^{2} (-1)^m A_{2-m}T_{2m}e^{im\omega_0 t}\end{aligned} \tag{6}$$

In this rotating frame the Hamiltonian is modulated by the Larmor frequency and its harmonics. According to the average Hamiltonian theory [15–17], the zero-order and first-order average Hamiltonian of eqn. (6) are given by

$$\mathscr{H}^{(0)} = \frac{1}{\tau_0}\int_0^{\tau_0}\mathscr{H}(t)\,\mathrm{d}t \tag{7a}$$

$$\mathscr{H}^{(1)} = \frac{-i}{2\tau_0}\int_0^{\tau_0}\mathrm{d}t_1\int_0^{t_1}\mathrm{d}t_2[\mathscr{H}(t_1), \mathscr{H}(t_2)] \tag{7b}$$

where $\tau_0 = 2\pi/\omega_0$, the Larmor precession period.

For most internal spin interactions the zero-order average Hamiltonian is already a very good approximation to the time-dependent Hamiltonian given in eqn. (6), since the Zeeman term is usually large enough to truncate the internal spin interactions. However, for half-integer quadrupolar nuclei, the quadrupolar coupling constants are often so large that the Zeeman interaction cannot effectively truncate the quadrupolar interaction. This situation is similar to that discussed by VanderHart [18] for the CSA interaction in low magnetic field. In such cases, higher order effects have to be taken into account when transforming the total Hamiltonian from the laboratory frame to the rotating frame. Inserting eqn. (6) into eqn. (7) yields the total average Hamiltonian up to the first-order approximation in the rotating frame,

$$\begin{aligned}\mathscr{H} &= A_{20}T_{20}\\ &\quad + \frac{\omega_Q^2}{2\omega_0}\sum_{m\neq 0}\frac{1}{m}(A_{2m}A_{2-m}[T_{2m}, T_{2-m}]\\ &\quad + A_{2m}A_{20}[T_{2m}, T_{20}])\end{aligned} \tag{8}$$

The first term in eqn. (8) is the same as the first-order correction given by the perturbation theory. The second term is made up of two parts: a secular part (which commutes with the Zeeman Hamiltonian) and a non-secular part (which does not commute with the Zeeman Hamiltonian). As we will discuss, the secular part in the second term corresponds to the second-order correction of the eigenvalues.

The presence of the non-secular term in the total Hamiltonian raises three issues. The first is why such a term exists in the first-order average Hamiltonian. The next concerns its contribution to the evolution of the spin system, and the final question is how to handle this non-secular term during the evolution of the density matrix. The answers to all these questions are related to the original assumptions of the average Hamiltonian theory [17]. According to the perturbation theory, the exact eigenvalues and eigenfunctions of the total Hamiltonian are gradually approached by adding higher order corrections to the energy levels and the eigenfunctions of the perturbed Hamiltonian [19]. On the other hand, in the average Hamiltonian theory we first transform the total Hamiltonian from the Schrödinger representation to an interaction representation based on the Zeeman Hamiltonian. The total Hamiltonian in the interaction representation becomes a periodic function of time with period τ_0, and we then concentrate only on the behavior of the density matrix at times $n\tau_0$ during its evolution. The elements of the density matrix at these periodic points are approximately given by an average Hamiltonian which is time independent and which discards the exact evolution during a cycle. The average Hamiltonian theory thus provides a *stroboscopic* description of the time evolution of the density matrix under the total Hamiltonian. The average Hamiltonian can be approached by adding higher order corrections, which contain multiple time integrals over the products of the time-dependent Hamiltonian and which include all contributions from fast to slow variations of the density matrix. Therefore the average Hamiltonian in general is not diagonal. If we are only interested in the slowest variation of the density matrix in the n-th order correction, we may simply drop the non-secular part. Such a treatment of the average Hamiltonian corresponds to the secular average Hamiltonian theory [15,20–22].

We now return to the derivation of the first-order average Hamiltonian. For half-integer spins ($I > \frac{1}{2}$) only the central transition ($-\frac{1}{2} \leftrightarrow \frac{1}{2}$) can be observed in FT-NMR experiments when the quadrupolar coupling constant is much larger than the rf field strength. Since the zero-order term in the average Hamiltonian does not alter this transition frequency it can be ignored, and therefore from now on we need only focus on the secular part of the first-order term in the average Hamiltonian. Using the product properties of irreducible tensors [23,24], this contribution may be rewritten as

$$\mathcal{H}^{(1)} = \sum_{l'=1,3} \sum_{l=0}^{4} \sigma_{ll'} A_{l0} T_{l'0} \qquad (9)$$

The A_{l0}, T_{l0} terms in eqn. (9) are the spatial and spin parts, respectively, of the l-th rank irreducible tensors arising from the direct product of two second-order irreducible tensors. The $\sigma_{ll'}$ represent the coupling constants of the second-order quadrupolar interaction arising from the first-order average Hamiltonian. These values are

$$\sigma_{ll'} = (-1)^{l'} W(2, 2, I, I; l', I) \frac{5\omega_Q^2 \langle I | T_2 | I \rangle^2}{\omega_0 \langle I | T_{l'} | I \rangle} \times \sum_{m \neq 0} \frac{1}{m} C(2, 2, l, m, -m, 0) \times C(2, 2, l', m, -m, 0) \qquad (10)$$

where

$$\langle I | T_l | I \rangle = l! \left[\frac{(2I+l+1)!}{(2l)!(2I-l)!} \right]^{1/2} \qquad (11)$$

and

$$\langle Im | T_{lq} | Im' \rangle = \langle I | T_l | I \rangle \sqrt{\frac{2l+1}{2I+1}}\, C(I, l, I; m, q, m') \qquad (12)$$

In eqn. (10), $C(l_1, l_2, l; m_1, m_2, m)$ are the Clebsch–Gordan coefficients, $W(2, 2, I, I; l', I)$ are $6-j$ symbols, I is the nuclear spin, and l, l' are the tensor ranks. The values of $\langle I | T_l | I \rangle$, $W(2, 2, I, I; l', I)$, and $\sigma_{ll'}$ for $I = \frac{3}{2}$, $\frac{5}{2}$, and $\frac{7}{2}$ are listed in Tables 1, 2, and 3, respectively.

Since the quadrupolar coupling tensor is a real and symmetric operator, the odd rank irreducible tensors A_{l0} are zero. Among the remaining terms in eqn. (9), $A_{0,0}$ is a scalar operator whose value reflects the second-order isotropic shift of the quadrupolar interaction, and A_{20} and A_{40} are

TABLE 1

Values of $\langle I | T_l | I \rangle$

	$l=1$	$l=2$	$l=3$
$I=\frac{3}{2}$	$\sqrt{5}$	$\sqrt{6}$	$3\sqrt{2}$
$I=\frac{5}{2}$	$\sqrt{\frac{35}{2}}$	$2\sqrt{14}$	$9\sqrt{2}$
$I=\frac{7}{2}$	$\sqrt{42}$	$6\sqrt{7}$	$3\sqrt{165}$

TABLE 2

Value of W (2, 2, I, I, l, I) coefficients

	$I=\frac{3}{2}$	$I=\frac{5}{2}$	$I=\frac{7}{2}$
$l=1$	$-\frac{1}{5\sqrt{2}}$	$-\frac{1}{5\sqrt{7}}$	$-\frac{1}{2\sqrt{105}}$
$l=3$	$\frac{1}{5\sqrt{2}}$	$\frac{9}{70\sqrt{2}}$	$\frac{1}{14}\sqrt{\frac{11}{15}}$

orientationally dependent. Their principal values are given by

$$\rho_{00}=\frac{\delta_Q^2(3+\eta_Q^2)}{2\sqrt{5}} \tag{13a}$$

$$\rho_{20}=-\frac{\delta_Q^2(3-\eta_Q^2)}{\sqrt{14}}, \quad \rho_{2\pm1}=0,$$

$$\rho_{2\pm2}=\sqrt{\tfrac{3}{7}}\,\eta_Q\delta_Q^2 \tag{13b}$$

$$\rho_{40}=\frac{\delta_Q^2\left(9+\dfrac{\eta_Q^2}{2}\right)}{\sqrt{70}}, \quad \rho_{4\pm1}=0,$$

$$\rho_{4\pm2}=\frac{3}{2\sqrt{7}}\eta_Q\delta_Q^2,$$

$$\rho_{4\pm3}=0, \; \rho_{4\pm4}=\tfrac{1}{4}(\eta_Q\delta_Q)^2 \tag{13c}$$

The orientation dependence of the spatial irreducible tensor $A_{l,m}$ can therefore be explicitly represented using the Wigner rotation matrices $\mathscr{D}^{(l)}_{m',m}(\alpha, \beta, \gamma)$ and the principal values as

$$A_{lm}=\sum_{m'=-l}^{l}\mathscr{D}^{(l)}_{m',m}(\alpha, \beta, \gamma)\rho_{lm'} \tag{14}$$

where α, β, γ are the three Euler angles relating the transformation to the laboratory frame from the PAS of the quadrupolar interaction.

TABLE 3

Values of $\sigma_{ll'}$

	ll			
	21	23	41	43
$I=\frac{3}{2}$	$-\frac{6}{5\sqrt{14}}$	$\frac{6}{\sqrt{35}}$	$\frac{18}{5\sqrt{70}}$	$\frac{17}{5\sqrt{7}}$
$I=\frac{5}{2}$	$-\frac{16}{5\sqrt{14}}$	$\frac{6}{\sqrt{35}}$	$\frac{48}{5\sqrt{70}}$	$\frac{17}{5\sqrt{7}}$
$I=\frac{7}{2}$	$-\frac{6}{\sqrt{14}}$	$\frac{6}{\sqrt{35}}$	$\frac{18}{\sqrt{70}}$	$\frac{17}{5\sqrt{7}}$

Using eqns. (9) and (10) as well as the properties of the Clebsch–Gordan and $6-j$ coefficients, the central transition frequencies of quadrupolar nuclei become

$$\omega^{(2)}_{\frac{1}{2}\leftrightarrow-\frac{1}{2}}=\sum_{l=0,2,4}C_l A_{l,0} \tag{15}$$

where

$$C_l=\omega_Q^{(2)}[C(2, 2, l, 2, -2)+2C(2, 2, l, 1, -1)] \tag{16}$$

and

$$\omega_Q^{(2)}=\frac{\omega_Q^2}{\omega_0}(I-\tfrac{1}{2})(I+\tfrac{3}{2}) \tag{17}$$

As can be seen from eqn. (15), the orientation dependence of the central transition frequencies can be expanded in second- and fourth-rank tensors, and the $\omega_Q^{(2)}$ in the coefficients, C_l, is now defined as the second-order quadrupolar coupling constant.

When the sample rotates around an axis inclined at an angle of β_r relative to the external magnetic field, the central transition frequencies become time dependent. Since the sample rotation operator commutes with the spin operators in the Hamiltonian, the time dependence of the transition frequencies is given simply by

$$\omega^{(2)}_{\frac{1}{2}\leftrightarrow-\frac{1}{2}}=\sum_{l=0,2,4}\sum_{m=-l}^{l}C_l\mathscr{D}^{(l)}_{m,0}[\Omega^{\mathrm{SFC}}(t)]A_{l,m} \tag{18}$$

where $\Omega^{\mathrm{SFC}}(t)$ are the three Euler angles of the transformation to the laboratory frame from a sample-fixed-coordinate (SFC) frame. If the sample spinning axis is fixed in the laboratory frame, the explicit expression for $\Omega^{\mathrm{SFC}}(t)$ is

$$\Omega^{\mathrm{SFC}}(t)=(\omega_r t+\alpha_0, \theta, \gamma_0) \tag{19}$$

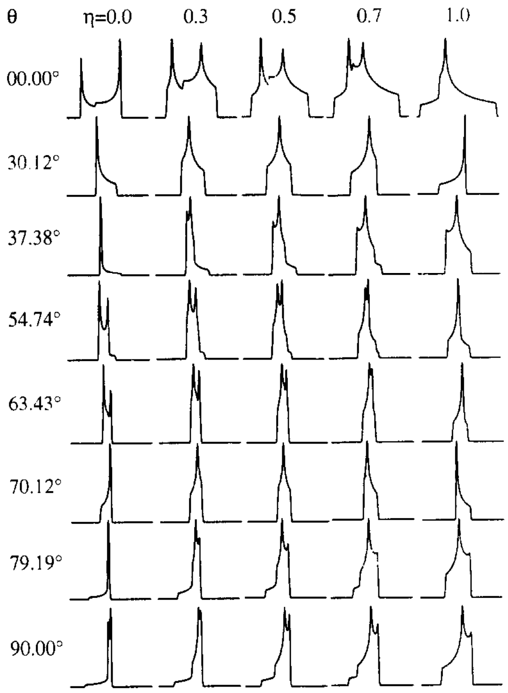

Fig. 1. Powder lineshapes arising from the second-order effect of an $I = \frac{3}{2}$ quadrupolar interaction under fast spinning about a single axis tilted at different angles. Spectra are shown for different values of the asymmetry parameter, η_Q.

where ω_r is the sample spinning speed, α_0 and γ_0 are the initial rotor phases, and θ is the angle of the spinning axis with respect to the magnetic field.

If the spinning speed is much larger than the amplitude of the second-order quadrupolar interaction, $\omega_Q^{(2)}$, then the rapidly oscillating time-dependent terms are averaged to zero. Under these circumstances, powder lineshapes are determined only by the time-independent term in eqn. (18). Figure 1 shows the variation of the simulated quadrupolar powder lineshapes with different asymmetry parameters (η_Q) and different angles of the sample spinning axis.

Dynamic angle spinning (DAS) and double rotation (DOR)

It is well known that first-order inhomogeneous broadenings originating from the chemical shift anisotropy can be efficiently averaged by magic-angle spinning [4,5]. However, applying MAS to a powder sample whose principal broadening arises from the second-order quadrupolar interaction reduces the linewidth by only a factor of $1/P_4(\cos\theta^{(2)}) = 2.57$. Even under variable angle spinning (VAS) there is no solution which completely eliminates the second-order broadening, since the lineshapes are determined by both second- and fourth-rank spatial tensors simultaneously. Under the fast spinning condition, the coefficients of the second- and fourth-rank tensors are second- and fourth-order Legendre polynomials, $P_2(\cos\theta)$ and $P_4(\cos\theta)$. As can be seen from Fig. 2, the node of P_2 is $\theta^{(2)} = 54.74°$, and the nodes of P_4 are $\theta_1^{(4)} = 30.56°$ and $\theta_2^{(4)} = 70.12°$ in the interval of [0°, 90°]. There are no common nodes for P_2 and P_4, and hence sample spinning about only a single axis cannot eliminate all anisotropic broadening in central transitions of quadrupolar nuclei.

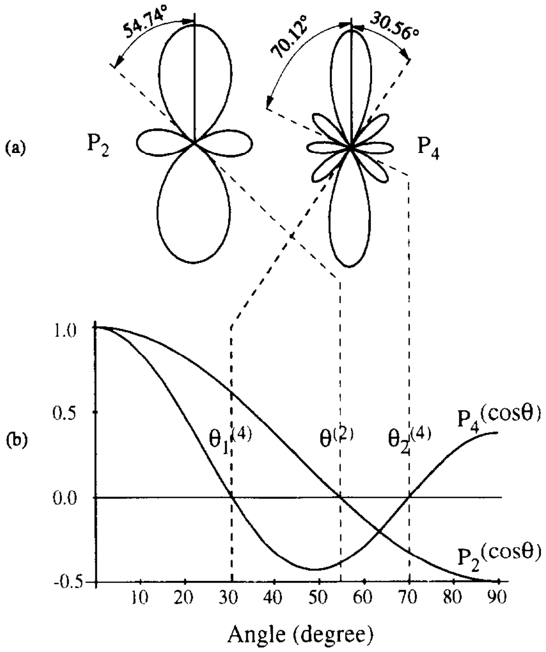

Fig. 2. Plot of the second- and fourth-order Legendre polynomials, $P_2(\cos\theta)$ and $P_4(\cos\theta)$, *versus* the angle of the rotation axis in VAS. (a) Plot in polar coordinates, (b) in Cartesian coordinates. The nodes of P_2 and P_4 are indicated by the dashed line.

According to eqn. (17), the second-order quadrupolar coupling constant, $\omega_Q^{(2)}$, is inversely proportional to the Larmor frequency ω_0. The overall second-order quadrupolar broadening consequently will decrease as the magnetic field is increased. As an example, consider a quadrupolar nucleus with a coupling constant $\omega_Q = 100$ kHz (a typical value for a spin $\frac{3}{2}$ nucleus). In order to achieve 1 Hz linewidths in the spectrum, the Larmor frequency, ω_0, of the nucleus has to be of the order of $\omega_Q^2 \sim 10$ GHz, corresponding to a magnetic field between 10^3 and 10^4 T for typical gyromagnetic ratios. It is obviously impossible to obtain such high magnetic fields with current technology, and so eliminating the second-order broadening simply by increasing the external magnetic field is not presently feasible.

Dynamic angle spinning (DAS)

An alternative way to look for a solution which eliminates quadrupolar broadening is to examine the frequency variations of the local magnetization under rapid rotation. Figure 3 shows how the central transition frequencies vary as a function of the spinning axis angle, θ, defined relative to the external magnetic field. The initial frequency of each line in Fig. 3a corresponds to a particular orientation of the quadrupolar PAS chosen randomly in the SFC frame. As can be seen, the central transition frequency of each quadrupolar spin oscillates as the sample spinning axis angle changes from 0.00° to 90°. The oscillations are also dependent on the orientation of the PAS in the SFC frame. However, if each line in Fig. 3a is divided by the value of its first point (corresponding to $\theta = 0.00°$), all the lines converge at two points: one at $\theta = 0.00°$, and the other at $\theta = 63.43°$. Such a convergence tells us that, although the central transition frequencies vary differently with θ, there are two angles, $\theta = 0.00°$ and $\theta = 63.43°$, at which the central transition frequencies are proportional to each other. The coefficient of proportionality is a negative number. If the total magnetization precesses with frequencies determined by the orientation of the quadrupolar PAS in the SFC frame at $\theta = 0.00°$, the precession will reverse once the sample spinning axis flips from $\theta = 0.00°$ to $\theta = 63.43°$. The only difference is that the precession frequencies are changed by a factor of 5 (see Fig. 3b), but this scaling factor can be compensated for by allowing the magnetization to evolve five times longer at $\theta = 63.43°$ than at $\theta = 0.00°$. The total magnetization will then refocus into a DAS echo, and the anisotropic broadening can thus be completely eliminated. In fact, such behavior may also occur if each line is divided by the frequency at other θ values of the spinning axis. Figure 3c shows a second pair of angles of the spinning axes, $\theta_1 = 37.38°$ and $\theta_2 = 79.19°$, which will refocus the second-order

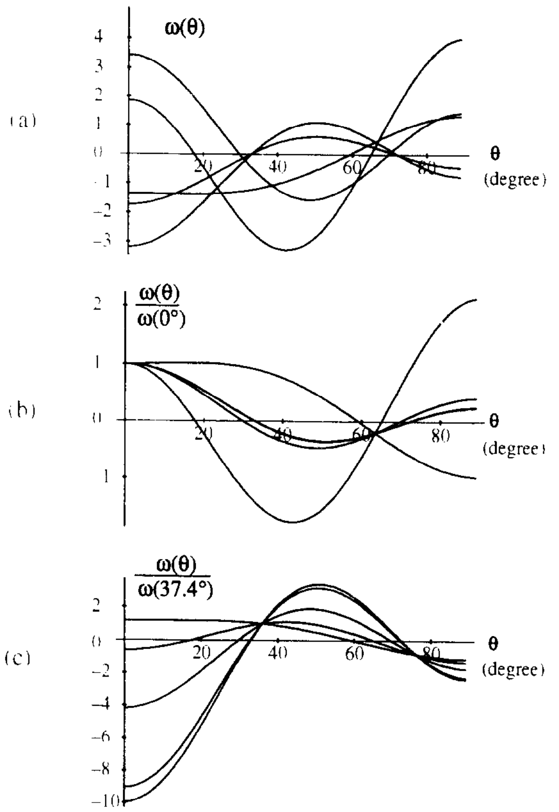

Fig. 3. Variation of the second-order shifts with the angle of the sample spinning axis relative to the external field. (a) Frequency dependence. Each line corresponds to a particular crystal orientation chosen randomly in the SFC. (b) After each line in (a) is divided by its first point, corresponding to $\theta = 0°$, all shifts refocus for $\theta_1 = 0°$, $\theta_2 = 63.43°$, and $\omega_1 = -5\omega_2$. (c) Same as (b), but divided by the value at $\theta_1 = 37.38°$. All lines then refocus at $\theta_2 = 79.19°$ and $\omega_1 = -\omega_2$ for all spins.

quadropolar interaction with a scaling factor of 1. In addition, it can be shown that there are no convergences and therefore no solutions present when each line is divided by any frequency between $\theta = 39.23°$ and $\theta = 63.43°$.

We can set up an experiment in which the sample is spinning at one angle, θ_1, during the first evolution time, t_1, and at another angle, θ_2, during the second evolution time, t_2. This is achieved by suddenly flipping the rotation axis of the sample from θ_1 to θ_2 between t_1 and t_2, in an experiment called dynamic angle spinning [7]. From eqn. (18), the total evolved phase of the magnetization at the end of the second evolution time t_2 is

$$\varphi(t_1, t_2) = \int_0^{t_1} \omega^{(2)}_{\frac{1}{2}\leftrightarrow-\frac{1}{2}}\left[\Omega_{r_1}(t)\right] \mathrm{d}t + \int_{t_1}^{t_1+t_2} \omega^{(2)}_{\frac{1}{2}\leftrightarrow-\frac{1}{2}}\left[\Omega_{r_2}(t)\right] \mathrm{d}t \qquad (20)$$

where the two sets of Euler angles are defined by

$$\Omega_{r_1}(t) = \Omega(\omega_r t + \phi_1, \theta_1, \gamma_1) \qquad (21a)$$

$$\Omega_{r_2}(t) = \Omega(\omega_r t + \phi_2, \theta_2, \gamma_2) \qquad (21b)$$

We assume that the spinning speeds during different evolution times are the same, and take ϕ_1 and ϕ_2 as the initial phases of the azimuth angle at the beginning of the two evolution times. γ_1 and γ_2 are the initial phases of the rotation axis relative to the laboratory frame. Owing to the cylindrical symmetry of the magnetization around the external field H_0, γ_1 and γ_2 may be set equal to zero.

When the sample spinning speed (ω_r) is much larger than $\omega_Q^{(2)}$, the total evolved phase of the magnetization is only determined by the terms which are linearly dependent on time in eqn. (20):

$$\varphi(t_1, t_2) = \sum_{l=2,4} C_l\left[d^{(l)}_{0,0}(\theta_1)t_1 + d^{(l)}_{0,0}(\theta_2)t_2\right]A_{l,0} \qquad (22)$$

To eliminate the anisotropic shifts from the central transition, we simply set the total evolved phase of the magnetization, $\varphi(t_1, t_2)$, equal to zero, yielding

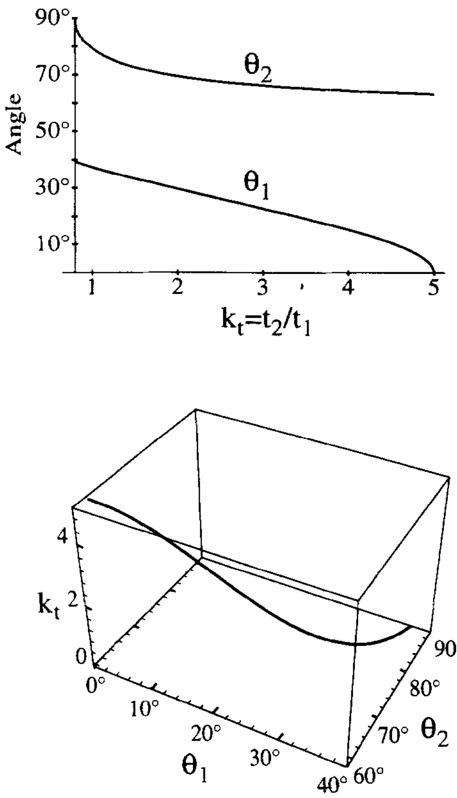

Fig. 4. Graphic representation of DAS complementary angles [from eqns. (23a) and (23b)] as a function of the time ratio $k_t = t_1/t_2$. (a) Individual plots of θ_1 and θ_2 *versus* k_t. (b) Three-dimensional plot of the DAS angles, with the time ratio k_t.

$$P_2(\cos\theta_1)t_1 + P_2(\cos\theta_2)t_2 = 0 \qquad (23a)$$

$$P_4(\cos\theta_1)t_1 + P_4(\cos\theta_2)t_2 = 0 \qquad (23b)$$

in which we have replaced $d^{(l)}_{0,0}$ by Legendre polynomials P_l (since $d^{(l)}_{0,0} = P_l$). The two pairs of angles shown in Figs. 3b and 3c exactly satisfy the simultaneous Eqns. (23a) and (23b). Other solutions are shown schematically in Fig. 4. In Fig. 4a, θ_1 and θ_2 are each plotted separately as a function of the time ratio $k_t = t_2/t_1$. In fact, eqns. (23a) and (23b) have two sets of solutions: one is related to k_t and the other to $1/k_t$. The analytic solutions corresponding to the curves in Fig. 4 are

$$\cos^2(\theta_1) = \tfrac{1}{3}\left(1 \pm \frac{2}{\sqrt{5}}\sqrt{k_t}\right) \tag{24a}$$

$$\cos^2(\theta_2) = \tfrac{1}{3}\left(1 \mp \frac{2}{\sqrt{5}} \cdot \frac{1}{\sqrt{k_t}}\right) \tag{24b}$$

Each pair of rotation axis angles given by eqns. (24a) and (24b) are called DAS complementary angles.

A few pairs of DAS complementary angles are listed in Table 4. From Fig. 1, the lineshape at θ_1 is the mirror image of that at θ_2 about the isotropic shift scaled by k_t. The first pair of DAS complementary angles, $\theta_1 = 0.00°$ and $\theta_2 = 63.43°$, in Table 4 has the maximum scaling factor ($k_t = 5$), which requires the shortest time spent at $\theta_1 = 0.00°$, The second pair consists of the magic angles of the fourth-order Legendre polynomial $P_4(\cos\theta)$, $\theta_1 = 30.56°$ and $\theta_2 = 70.12°$, where $k_t = 1.87$. The third pair is usually used for the DAS experiment with $k_t = 1$, corresponding to $\theta_1 = 37.38°$ and $\theta_2 = 79.19°$.

It is well known that the MAS trajectory can be thought of as the path traversed by the magnetic field on a cone in an octahedron in the SFC frame. The base of the cone passes through three vertices of the octahedron, and the apex of the cone is at the center of the octahedron (see Fig. 5a). Similarly, the DAS trajectory with $k = 1$ can also be thought of as a path on two cones whose bases pass through the vertices of a dodecahe-

TABLE 4

Angles in an icosahedron or a dodecahedron [a]

k_t	Angle	Dodecahedron	Icosahedron	$\cos^2\theta$	$P_2(\theta)$	$P_4(\theta)$
5	0°	$\widehat{\vec{Z}\vec{Z}}$	$\widehat{\vec{Z}\vec{Z}}$	1	1	1
	63.43°	$\widehat{\vec{Z}\vec{P}_C}$	$\widehat{\vec{Z}\vec{V}_1}$	$\frac{1}{5}$	$-\frac{1}{5}$	$-\frac{1}{5}$
$\frac{49}{59-6\sqrt{30}}$	30.56°	–	–	$\frac{15+2\sqrt{30}}{35}$	$\frac{5-3\sqrt{30}}{35}$	0
	70.12°	–	–	$\frac{15-2\sqrt{30}}{35}$	$\frac{5+3\sqrt{30}}{35}$	0
1	37.38°	$\widehat{\vec{Z}\vec{V}_1}$	$\widehat{\vec{Z}\vec{T}_{C_1}}$	$\frac{\sqrt{5}+2}{3\sqrt{5}}$	$\frac{1}{\sqrt{5}}$	$-\frac{\sqrt{5}}{9}$
	79.19°	$\widehat{\vec{Z}\vec{V}_2}$	$\widehat{\vec{Z}\vec{T}_{C_2}}$	$\frac{\sqrt{5}-2}{3\sqrt{5}}$	$\frac{-1}{\sqrt{5}}$	$\frac{\sqrt{5}}{9}$
$\frac{4}{5}$	39.23°	–	–	$\frac{3}{5}$	$\frac{2}{5}$	$\frac{3}{10}$
	90°	$\widehat{\vec{Z}\vec{E}_{C_3}}$	$\widehat{\vec{Z}\vec{E}_{C_3}}$	0	$-\frac{1}{2}$	$\frac{3}{8}$
$\frac{9}{5}$	31.09°	–	–	$\frac{11}{15}$	$\frac{3}{5}$	$-\frac{1}{45}$
	70.53°	$\widehat{\vec{V}_1\vec{V}_3}$	$\widehat{\vec{T}_{C_1}\vec{T}_{C_3}}$	$\frac{1}{9}$	$-\frac{1}{3}$	$\frac{1}{81}$
$\frac{7+3\sqrt{5}}{8}$	31.72°	$\widehat{\vec{Z}\vec{E}_{C_1}}$	$\widehat{\vec{Z}\vec{E}_{C_1}}$	$\frac{\sqrt{5}+1}{2\sqrt{5}}$	$\frac{\sqrt{5}+3}{4\sqrt{5}}$	$-\frac{3-\sqrt{5}}{16}$
	71.03°	–	–	$\frac{\sqrt{5}-1}{5+3\sqrt{5}}$	$\frac{5-3\sqrt{5}}{5}$	$\frac{4\sqrt{5}-9}{2}$

[a] V is the vertices of the dodecahedron and icosahedron, and E_C is the centers of the edges, T_C is the centers of the triangles, and P_C is the centers of the pentagons. Latin letters in the indices are used to distinguish different centers (see Fig. 5).

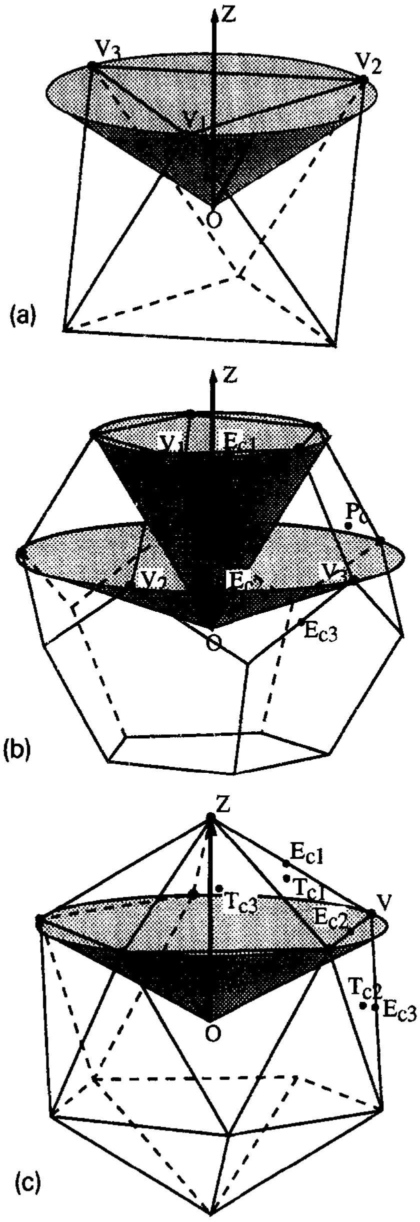

Fig. 5. The external magnetic field, as viewed in the SFC, travels on one or two cones, depending on whether the rotation is MAS or DAS. (a) The magic-angle cone crosses three vertices of an octahedron in MAS. (b) Two DAS cones cross ten vertices of a dodecahedron in the $k_t = 1$ case, while (c) is the DAS trajectory on an icosahedron. V is used to label a vertex; P denotes pentagon, T denotes triangle, E denotes edge, and C denotes center. Latin letters are used in the indices to distinguish different centers.

dron, and whose apexes are at the center of the dodecahedron in the SFC frame (see Figs. 5b and 5c). Other solutions of the DAS trajectory also relate to both a dodecahedron and an icosahedron. The symmetry of the DAS trajectory is therefore determined by the icosahedral group [6]. The physical position of the DAS complementary angles listed in Table 4 on either an icosahedron or a dodecahedron are specified in the table and Figs. 5b and 5c.

The isotropic portion of the spin Hamiltonian obviously will not be affected by flipping the rotation axis between the two evolution periods. Experimentally, the free induction decay (fid) points are acquired at the peaks of the DAS echos formed by incrementing t_1 and t_2. The amplitude of these echos will therefore be modulated by the isotropic resonance frequencies of the nuclear spins. After Fourier transformation of the fid, a high resolution spectrum can be obtained.

Once the spinning speed is comparable to $\omega_Q^{(2)}$, the contribution of other time-dependent terms in eqn. (20) has to be take into account in the total evolved phase of the magnetization. If the fid is acquired on the DAS echo peaks, then [from eqns. (24a) and (24b)] we have $t_2 = k_t t_1$ within the range $4/5 \leq k_t \leq 5$. Thus using the Wigner rotation matrices and eqns. (18), (20) and (21), the net evolved phase of the magnetization at time $t = t_1 + t_2$ can be written as

$$\varphi^{\mathrm{DAS}}(t) = \sum_{m \neq 0} \mathrm{e}^{-im\alpha}\Big[B_m^{\mathrm{DAS}}(\theta_2)\, \mathrm{e}^{-im(\phi+\omega_r t)} \times \psi(-k_t t) - B_m^{\mathrm{DAS}}(\theta_1)\psi(t)\Big] \qquad (25)$$

where

$$B_m^{\mathrm{DAS}}(\theta) = \sum_{l=2,4} \frac{iC_l A_{l,m}}{m\omega_r} d_{m,0}^{(l)}(\theta), \; |m| \leq l$$

$$\psi(t) = 1 - \exp\left(-i\frac{m\omega_r t}{1+k_t}\right) \qquad (26)$$

Later we will see that eqn. (25) accounts for DAS sidebands.

Double rotation (DOR)

A second method for narrowing quadrupolar patterns is double rotation [9–11]. After applying a rotation about a fixed axis at a particular angle with respect to the magnetic field, the Hamiltonian will be truncated along the rotation axis if the spinning speed is fast enough ($\omega_r \gg \omega_Q^{(2)}$). The residual portions are then proportional to the Legendre polynomials $P_l(\cos\theta)$ (in our case, $l = 2,4$). For example, if the applied rotation is MAS, the residual lineshape of the central transition for a powder sample is uniquely determined by the fourth-order Legendre polynomial, $P_4(\cos\theta)$. The linewidth will be reduced by a factor of $1/P_4(\cos\theta_m^{(2)}) = 2.57$ where $\theta_m^{(2)} = 54.74°$. In the variation of $P_2(\cos\theta)$ and $P_4(\cos\theta)$ with θ, there are no angles for which the values of $P_2(\cos\theta)$ and $P_4(\cos\theta)$ are equal to zero simultaneously (see Fig. 2). However, since the linewidth of a powder pattern varies with changes in the angle of rotation (see Fig. 1), it can be further narrowed by applying another rotation relative to the first. In other words, the linewidths of the powder patterns can be continuously narrowed to any degree by simultaneously applying the proper multiple rotations. Solutions can in fact be found which completely eliminate the second-order broadening with two rotations. One of these corresponds to the DOR method, in which the first rotation is performed about the magic angle $\theta_m^{(2)}$ with respect to the external magnetic field while the second rotation occurs about one of the magic angles $\theta_m^{(4)}$ of the fourth-order Legendre polynomial $P_4(\cos\theta)$.

After applying two rotations to eqn. (15) by using two iterations of eqn. (14), the transition frequency between two central levels ($m = \pm\frac{1}{2}$) becomes

$$\omega^{(2)}_{\frac{1}{2}\leftrightarrow-\frac{1}{2}}(t) = \sum_{l=0,2,4} C_l \sum_{m_1,m_2=-l}^{l} \mathscr{D}^{(l)}_{m_1,0}[\Omega_{r1}(t)] \times \mathscr{D}^{(l)}_{m_2,m_1}[\Omega_{r2}(t)] A_{lm_2} \qquad (27)$$

where C_l is given by eqn. (16). $\Omega_{r1}(t)$, $\Omega_{r2}(t)$ are

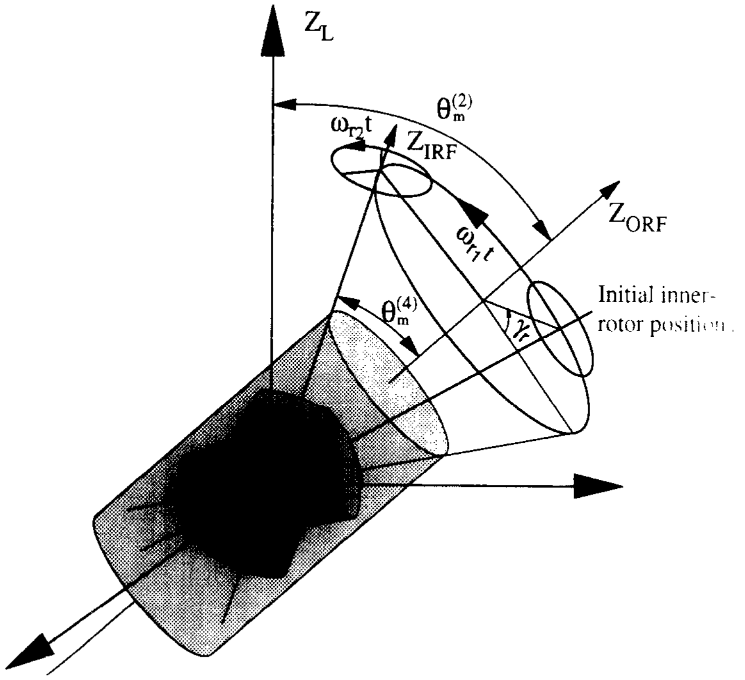

Fig. 6. Scheme for the coordinate transformation involving the laboratory frame, the outer rotor frame, and the inner rotor frame. The rotation axis of the outer rotor is tilted at the magic angle, $\theta_m^{(2)} = 54.74°$, of the second-order Legendre polynomial, while the inner rotor spins around $\theta_m^{(4)} = 30.56°$, one of the magic angles of the fourth-order Legendre polynomial.

two sets of Euler angles which define the transformations to the laboratory frame from the first, outer rotor frame (ORF), and to the outer rotor frame from the second, inner rotor frame (IRF), respectively. We assume that the spinning speeds of the outer and inner rotors are ω_{r_1} and ω_{r_2}, that the first rotation axis angle is β_{r_1} with respect to the external field, and that the second rotation axis angle is β_{r_2} relative to the first rotation axis. The initial phases of the first and second rotations are γ_{r_1} and γ_{r_2}, respectively. Explicit expressions for the two sets of Euler angles are therefore given by

$$\Omega_{r_1} = (\omega_{r_1} t + \alpha_{r_1}, \beta_{r_1}, \gamma_{r_1}) \tag{28a}$$

$$\Omega_{r_2} = (\omega_{r_2} t + \alpha_{r_2}, \beta_{r_2}, \gamma_{r_2}) \tag{28b}$$

As in MAS, the cylindrical symmetry of the external magnetic field H_0 allows us to set γ_{r_1} equal to zero. For a powder sample, the absolute orientation of each individual spin in the IRF is not important because each spin has equal probability of being at each orientation; hence we can also set α_{r_2} to zero. Finally, α_{r_1} and γ_{r_2} determine the relative phase γ_r between outer and inner rotors, which is given by $\gamma_r = \alpha_{r1} + \gamma_{r_2}$ (see Fig. 6).

After expanding eqn. (27), three terms result: the first term ($l = 0$) is a scalar, independent of both orientation and time; the second is dependent on orientation but independent of time; and the third depends on both orientation and time. Furthermore, since the Hamiltonian commutes with itself at all times, the total phase of the magnetization evolved after application of a 90° rf pulse is

$$\varphi^{\mathrm{DOR}}(t) = C_0 A_{0,0} t + \sum_{l=2,4} C_l \omega_l t + \sum_{m_1,m_2=-4}^{4} B^{\mathrm{DOR}}_{m_1,m_2} \times \mathrm{e}^{-i(m_1\gamma_r + m_2\alpha)} (\mathrm{e}^{-i(m_1\omega_{r_1} + m_2\omega_{r_2})t} - 1) \tag{29}$$

where

$$\omega_l = \sum_{m=-l}^{l} d^{(l)}_{-Nm,0}(\beta_{r_1}) d^{(l)}_{m,-Nm}(\beta_{r2}) A_{l,-Nm} \tag{30}$$

and

$$B^{\mathrm{DOR}}_{m_1,m_2} = \sum_{l=2,4} iC_l \frac{d^{(l)}_{m_1,0}(\beta_{r_1}) d^{(l)}_{m_2,m_1}(\beta_{r_2})}{m_1\omega_{r_1} + m_2\omega_{r_2}} \times \sum_{m'} d^{(l)}_{m',m_2}(\beta) \rho_{lm'} \, \mathrm{e}^{-im'\gamma} \tag{31}$$

with $N = \omega_{r_2}/\omega_{r_1}$. The Euler angles (α, β, γ) are used to describe the orientation of a single spin in the IRF. Eqns. (29) and (31) have to be subjected to the condition of $m_1 + m_2 \neq 0$ and $Nm_2 + m_1 \neq 0$. The first term in eqn. (29) corresponds to the isotropic shift in a powder sample, whereas the second term determines the linewidth and lineshape. The third term generates a set of DOR sidebands.

If we assume that the spinning speeds of both rotations are much larger than the amplitudes of the spin Hamiltonian $\mathscr{H}^{(1)}$ of the central transition, the third term in eqn. (31), $\varphi_l(t)$, becomes small enough to be neglected at all times. Since from the properties of Wigner rotation matrices we know that $d^{(l)}_{0,0}(\beta) = P_l(\cos\beta)$, we can eliminate the anisotropic shift, ω_l, in eqn. (29) if

$$P_2(\cos\beta_{r_1}) P_2(\cos\beta_{r_2}) = 0 \tag{32a}$$

$$P_4(\cos\beta_{r_1}) P_4(\cos\beta_{r_2}) = 0 \tag{32b}$$

and if $N = \omega_{r_2}/\omega_{r_1}$ is not an integer smaller than 5, present in eqn. (30). The solutions of eqns. (32a) and (32b) are $\beta_{r_1} = \theta^{(2)} = 54.74°$ and $\beta_{r_2} = \theta^{(4)} = 30.56°, 70.12°$, or *vice versa*. If N is an integer less than five, the residual broadening cannot be totally suppressed owing to interference between the two spinning speeds. Figure 7 shows the variation of the residual line broadenings in the central transition of a powder sample after application of DOR, for different ratios N. From this figure it can be seen that when the two spinning speeds are equal, $N = 1$, the linewidth of the centerband is about one tenth of the static linewidth, and will narrow with increasing ratios of the two spinning speeds. The linewidth reaches the order of the relaxation broadening, or of the higher order residual broadenings, when the ratio of the two spinning speeds is larger than 3. This means that the condition we gave earlier is not essential, and therefore the design of a double-

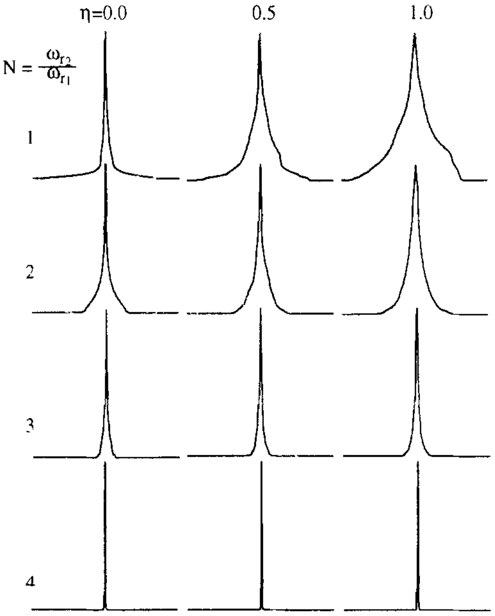

Fig. 7. Residual lineshapes of the centerband for the $I=\frac{3}{2}$ central transition under DOR. The quadrupolar coupling constant is 433 kHz. The ratio of the DOR two spinning speeds, $\omega_{r_2}/\omega_{r_1}$, and the asymmetry parameter η_Q are varied.

rotor probe should concentrate on increasing the spinning speed of the outer rotor.

Experimental results

Experimental DAS spectra of rubidium perchlorate ($RbClO_4$) were obtained using a home-built DAS probe [25] on a Chemagnetics spectrometer. The magnetic field was 11.7 T at which the resonance frequency of rubidium-87 is 163.6 MHz. The quadrupolar coupling constant, ω_Q, of the rubidium nucleus in rubidium perchlorate is 540 kHz and the asymmetry parameter, η_Q, is 0.1. The pulse sequence used was the same as in ref. 26. The central transition selective 90° pulses were ~ 4 μs, the recycle delays were ~ 1 s and the angle flipping times were ~ 30 ms.

DOR spectra of sodium oxalate were recorded with an improved home-built DOR probe [11] on a Bruker AM-400 spectrometer at 9.4 T with a resonance frequency of 105.8 MHz for sodium-23. The outer rotor was spun between 400 and 900 Hz while the inner rotor was spun at approximately 4000 Hz. The quadrupolar coupling constant of the sodium nucleus in sodium oxalate is 405 kHz, and the asymmetry parameter is 0.72. The selective 90° pulse was ~ 10 μs. A synchronized DOR experiment was implemented by monitoring the rotation of the outer rotor using a LED sensor, and the detected optical signal was converted into TTL pulses using a logic circuit. The TTL pulses were then used to trigger the pulse programmer of the spectrometer. By changing the triggering times, we were able to vary the rotor phase from 0° to 360°.

Figure 8 shows how the sideband intensities of DAS spectra vary with different spinning speeds in the case of $k_t = 1$, corresponding to $\theta_1 = 37.38°$

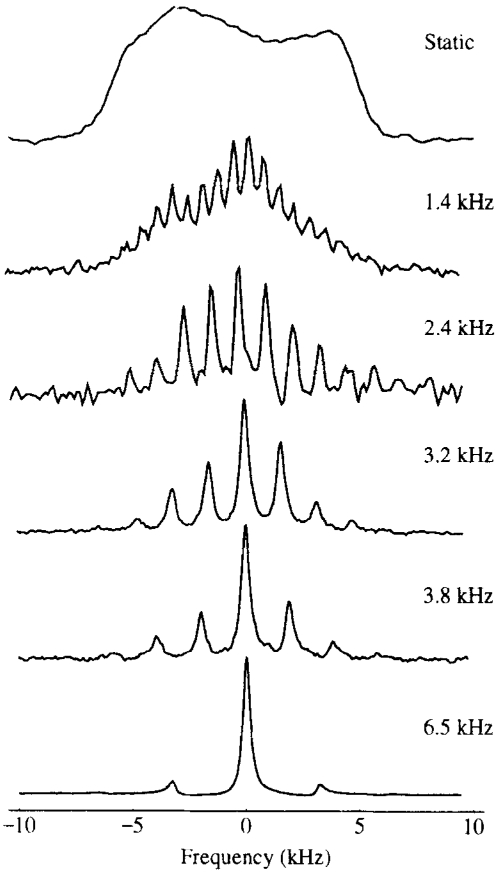

Fig. 8. Experimental DAS spectra of rubidium perchlorate ($RbClO_4$) with sidebands varying for different spinning speeds. The quadrupolar coupling constant of the rubidium nucleus is 540 kHz and the asymmetry parameter is 0.1.

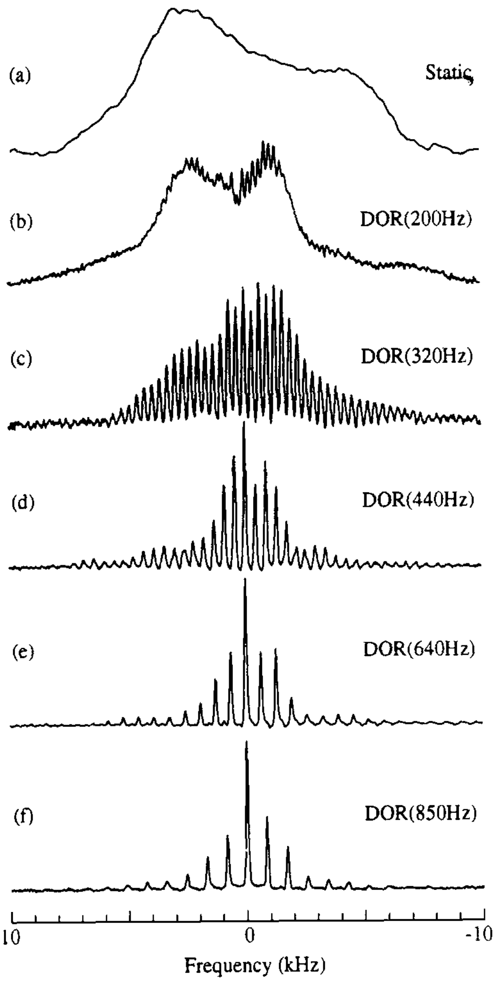

Fig. 9. Experimental variation of DOR sidebands in sodium-23 spectra of sodium oxalate, with different spinning speeds. The quadrupolar coupling constant is 405 kHz, the asymmetry parameter is 0.72, and the Larmor frequency is 105.8 MHz.

and $\theta_2 = 79.19°$. All sidebands are in phase and the difference between the nearest sidebands is one half of the spinning speed, but in general is dependent on the choice of k_t [27].

Figure 9 shows experimental spectra of sodium nuclei in sodium oxalate. It can be clearly seen that the spectra consist of high-resolution isotropic peaks accompanied by a train of sidebands like those under MAS. However, the envelope of sidebands does not mimic the static powder pattern (a characteristic observed in MAS spectra under slow spinning conditions). Rather, the envelope of sidebands arising from the first rotation (at the magic angle $\theta^{(2)}$) forms a P_4 lineshape, while the envelope associated with the second rotation (at $\theta^{(4)}$) forms a P_2 lineshape. The total sideband envelope is determined by the spinning speeds of both rotors, and is related to the convolution of the P_2 and P_4 lineshapes.

In addition, the frequency difference between two nearest sidebands in a MAS spectrum is uniquely determined by the spinning speed ω_r of the sample. In DOR spectra by contrast, there are a total of 81 different sets of sidebands, in principle. Each of them has a frequency difference, $m_1\omega_{r_1} + m_2\omega_{r_2}$, corresponding to a particular pair of m_1, m_2 values from -4 to 4. All sets of sidebands overlap each other and consequently make the pattern of sidebands complicated. Experimentally, though, since the inner rotor spins much faster than the outer rotor, the intensities of the sidebands are primarily determined by the outer rotor spinning speed.

Moment analysis

The moment analysis method was first proposed by Van Vleck [28] in order to characterize powder lineshapes in NMR spectra arising from homogeneous spin interactions, such as dipolar couplings between like nuclei. Later, Maricq and Waugh [12] applied this same method to analyze the sidebands in MAS spectra, and used the second and third moments to extract the chemical shift anisotropy parameters δ_{CSA} and η_{CSA}. Here we adapt a corresponding analysis for DAS and DOR sidebands, and similarly use moments to obtain the quadrupolar parameters.

The n-th moment is defined as

$$M_n = \int_{-\infty}^{\infty} \mathrm{d}\omega\,\omega^n G(\omega) = \sum_{N=-\infty}^{\infty} \omega_N^n I_N \tag{33}$$

where ω_N is the resonance frequency of the N-th sideband, and I_N is its intensity. $G(\omega)$ is the frequency spectrum given by $G(\omega) = \Sigma_N\ I_N \delta(\omega - \omega_N)$, resulting from Fourier transformation of the fid signal $G(t)$ without relaxation broadening. Once the spectrum is measured experimentally, the moments can be calculated by use of eqn. (33).

In order to relate the moments to the quadrupolar coupling parameters, it is possible to derive a relationship between the fid and the moments given by [29]

$$G(t) = \sum_{n=0}^{\infty} \frac{(-it)^n}{n!} M_n \tag{34}$$

By solving eqn. (34) for the n-th moment we get the following expression

$$M_n = i^n \frac{\mathrm{d}^n}{\mathrm{d}t^n} G(t)\,|_{t=0} \tag{35}$$

The fid is defined by

$$G(t) = \frac{1}{8\pi^2} \int_0^{2\pi} \int_0^{2\pi} \int_0^{\pi} \exp[-i\varphi(t)] \times \sin\beta \,\mathrm{d}\beta \,\mathrm{d}\gamma \,\mathrm{d}\alpha \tag{36}$$

in terms of the total evolved phase of the magnetization, $\varphi(t)$.

After inserting the total evolved phases, $\varphi^{\mathrm{DAS}}(t)$ and $\varphi^{\mathrm{DOR}}(t)$, of the magnetization given in eqns. (25) and (29), respectively, into eqn. (36), and then applying eqn. (35), expressions for the moments of DAS and DOR spectra can be obtained. The DAS and DOR moments are indeed quite similar in form, and, using properties of irreducible tensors, can be written as

$$M_0 = 1 \tag{37a}$$

$$M_1 = 0 \tag{37b}$$

$$M_2 = \sum_{l,m} a^{(1)}_{l,m} a^{(1)}_{l,-m} S(l) \tag{37c}$$

$$M_3 = \sum_{l_1,m_1} a^{(1)}_{l_1,m_1} \Bigg[3a^{(2)}_{l_1,-m_1} S(l_1) + \sum_{l_2,l_3,m_2} a^{(1)}_{l_2,m_2} a^{(1)}_{l_3,-m_1-m_2} S(l_1 l_2 l_3) \Bigg] \tag{37d}$$

$$M_4 = \sum_{l_1,m_1} \Bigg\{ \Big[3a^{(2)}_{l_1,m_1} a^{(2)}_{l_1,-m_1} + 4a^{(1)}_{l_1,m_1} a^{(3)}_{l_1,-m_1} \Big] S(l_1) + \sum_{l_2,l_3,m_2} a^{(1)}_{l_1,m_1} a^{(1)}_{l_2,m_2} \times \Bigg[6a^{(2)}_{l_3,-m_1-m_2} S(l_1 l_2 l_3) + \sum_{L,l_4,m_3} a^{(1)}_{l_3,m_3} a^{(1)}_{l_4,-m_1-m_2-m_3} S(L l_1 \cdots l_4) \Bigg] \Bigg\} \tag{37e}$$

The coefficients $S(L_1 \cdots L_{k-3} l_1, \cdots l_k)$ in the above equation relate to the zero-rank irreducible tensors (or scalar operators), $\rho_{00}(L_1 \cdots L_{k-3} l_1, \cdots l_k)$, through

$$S(L_1 \cdots L_{k-3} l_1, \cdots l_k) = C(l_1 l_2 L_1, m_1, m_2) \cdots \times C\left(L_{k-3}, l_{k-1}, l_k, \sum_{i=1}^{k-2} m_i, m_{k-1} \right) \times C\left(l_k l_k 0, \sum_{i=1}^{k-1} m_i, -\sum_{i=1}^{k-1} m_i \right) \times \rho_{00}(L_1 \cdots L_{k-3} l_1, \cdots l_k) \tag{38}$$

where $C(l_1 l_2 l_3, m_1 m_2)$ are the Clebsch–Gordan coefficients. The scalar operators $\rho_{00}(L_1 \cdots L_{k-3} l_1, \cdots l_k)$ arise from the product of k spatial irreducible tensors, S_{l_i,m_i} for $i = 1 \cdots k$, and the relationship with the principal values of the second-order quadrupolar coupling tensor, $\rho_{l,m}$, shown in eqn. (13) is

$$\rho_{00}(L_1 \cdots L_{k-3} l_1, \cdots l_k) = \sum_{m_1 \cdots m_k} C(l_1 l_2 L_1, m_1, m_2) \cdots \times C\left(L_{k-3}, l_{k-1}, l_k, \sum_{i=1}^{k-2} m_i, m_{k-1} \right) \times C\left(l_k l_k 0, \sum_{i=1}^{k-1} m_i, -\sum_{i=1}^{k-1} m_i \right) \rho_{l_1 m_1} \cdots \times \rho_{l_{k-1} m_{k-1}} \rho_{l_k, -\sum_{i=1}^{k-1} m_i} \tag{39}$$

The coefficients $a^{(i)}_{l,m}$ in eqn. (37) arise from the i-th derivative of the total evolved phase of the magnetization. The expressions for the DAS case are different from those for the DOR, namely

$$a_{l,m}^{(i)}(\mathrm{DAS}) = \left[\frac{m\omega_r}{1+k_t}\right]^i \frac{C_l}{m\omega_r}\left[k_t d_{m,0}^{(l)}(\theta_2)\ \mathrm{e}^{-im\phi} + d_{m,0}^{(l)}(\theta_1)\right] \tag{40a}$$

$$a_{l,m}^{(i)}(\mathrm{DOR}) = \sum_{m'=-l}^{l} \frac{C_l d_{m',0}^{(l)}\left(\theta_m^{(2)}\right) d_{m,m'}^{(l)}\left(\theta_m^{(4)}\right)}{m'\omega_{r_1} + m\omega_{r_2}} \times \mathrm{e}^{-im'\gamma_r}\left[m'\omega_{r_1} + m\omega_{r_2}\right]^i \tag{40b}$$

where ω_r, ω_{r_1}, and ω_{r_2} are the spinning speeds of the DAS rotor, the DOR outer rotor, and the DOR inner rotor, respectively. $d_{m',m}^{(l)}(\theta)$ are the reduced Wigner rotation matrix elements, and θ_1 and θ_2 are a pair of DAS complementary angles. $\theta_m^{(l)}$ are the magic angles of the l-th order Legendre polynomial, $P_l(\cos\theta)$.

As can be seen from eqns. (37) and (38), the n-th DAS and DOR moments are represented by a set of scalar operators, $\rho_{00}(L_1 \cdots L_{k-3} l_1, \cdots l_k)$, for $k = 2 \cdots n$. Actually, the representation of the n-th moment in terms of a set of scalar operators given in eqn. (39) holds for the non-spinning case as well. The difference is that the n-th moment of a static powder pattern only relates to a single scalar operator, which is a product of n second-order quadrupolar coupling tensors. Under sample rotation, the scalar operators present in the lower moments are multiplied by the spinning speeds and are folded into higher moments. From eqns. (40a) and (40b) the coefficients $a_{l,m}^{(i)}$ are independent of the spinning speed only if $i = 1$, and therefore only the second moment is the same as in the static case. In other words, the higher moments increase as the spinning speeds increase, and the parameter $\mu = M_4/M_2^2$, which characterizes the lineshapes, approaches infinity, resulting in high resolution peaks. It has been proven by Maricq and Waugh [12] that the third moments obtained from MAS spectra are also independent of the spinning speed owing to the symmetry properties of the Wigner rotation matrix elements, whereas the fourth moments increase as ω_r^2. The halfwidth of the envelope of the MAS sidebands therefore decreases according to a quasi-Lorentzian lineshape as the spinning speed increases. However, under DAS and DOR, the situation could be different since the second moment is independent of spinning speed. The third and higher moments may in general depend on the spinning speeds, although, for DOR the third moment is also independent of speed and relative phase. The fourth moment may have both linear and bilinear dependences on the spinning speeds. The parameter μ also increases with the spinning speeds both linearly and bilinearly; this means that the halfwidth of the envelope of the DOR and DAS sidebands decreases according to a quasi-super-Lorentzian lineshape, a feature that can be seen in Fig. 9.

The quadrupolar coupling parameters ω_Q and η_Q are encoded in the scalar operators. To extract these values, in practice it is necessary to evaluate the expressions explicitly in terms of δ_Q and η_Q as

$$\rho_{00}(l) = \frac{\delta_Q^4(3+\eta_Q^2)^2}{14\sqrt{2l+1}} \tag{41a}$$

$$\rho_{00}(222) = \frac{\delta_Q^6(27 - 135\eta_Q^2 + 45\eta_Q^4 - \eta_Q^6)}{98\sqrt{5}} \tag{41b}$$

$$\rho_{00}(224) = \rho_{00}(242) = \rho_{00}(422) = \frac{\delta_Q^6(162 - 243\eta_Q^2 + 144\eta_Q^4 + \eta_Q^6)}{980} \tag{41c}$$

$$\rho_{00}(244) = \rho_{00}(424) = \rho_{00}(442) = \frac{\delta_Q^6(81 + 162\eta_Q^2 + 9\eta_Q^4 + 4\eta_Q^6)}{49\sqrt{110}} \tag{41d}$$

$$\rho_{00}(444) = \frac{\delta_Q^6(2187 - 1863\eta_Q^2 + 1629\eta_Q^4 + 31\eta_Q^6)}{490\sqrt{715}} \tag{41e}$$

In general, all of the moments except the zeroth and first are dependent on the relative rotor phase γ_r under DOR and ϕ under DAS. Inserting eqns. (38), (40), and (41) into eqn. (37) yields the relationships of the second and third

DAS moments with the quadrupolar parameters and the relative rotor phase, ϕ, given by

$$M_2(\mathrm{DAS}) = \frac{\left[(3+\eta_\mathrm{Q}^2)\delta_\mathrm{Q}^2\omega_\mathrm{Q}^{(2)}\right]^2}{35} \times \sum_{m=0}^{4} c_m(k_t)\cos(m\phi) \qquad (42\mathrm{a})$$

$$M_3(\mathrm{DAS}) = \frac{-i3\times 10^{-4}\left[(3+\eta_\mathrm{Q}^2)\delta_\mathrm{Q}^2\omega_\mathrm{Q}^{(2)}\right]^2}{70} \times \sum_{m=0}^{4} s_m(k_t)\sin(m\phi) + \left[\delta_\mathrm{Q}^2\omega_2^{(2)}\right]^3 \sum_{m=0}^{4}\sum_{n=0}^{3} c_{m,n}(k_t)\eta_\mathrm{Q}^{2\mathrm{n}} \times\cos(m\phi) \qquad (42\mathrm{b})$$

where the coefficients $c_m(k_t)$, $c_{m,n}(k_t)$, and $s_m(k_t)$ are determined only by k_t. Their values for $k_t = 1$, 2, 3, 4, 5 are listed in Tables 5, 6, and 7. As can be seen from eqn. (42) and Table 7, the imaginary part of the third moment is dependent on the spinning speed only when $k_t \neq 1, 5$, as expected. Introduction of the relative rotor phase dependences in the DAS moment calculation does not introduce any new information, and only makes the whole expression more complicated. Experimentally, by randomly taking the relative phase at different times, the relative phase effects may be averaged out. This averaging process is equivalent to integrating over the relative phase in eqns. (37) to yield $m = 0$ in eqn. (42), and the third moment is independent of the spinning speed. Using eqn. (42), we have been able to determine the quadrupolar parameters from the experimental spectra shown in Fig. 8. The measured quadrupolar coupling constant varies between 537 and 570 kHz with different spinning speeds. This result agrees with the reported value (540 kHz) within an error of about seven percent.

Similarly using eqns. (37), (38), (40) and (41), the resulting second and third DOR moments are

$$M_2(\mathrm{DOR}) = \tfrac{23}{700}\left[(3+\eta_\mathrm{Q}^2)\delta_\mathrm{Q}^2\omega_\mathrm{Q}^{(2)}\right]^2 \qquad (43\mathrm{a})$$

$$M_3(\mathrm{DOR}) = 10^{-3}\left[\delta_\mathrm{Q}^2\omega_\mathrm{Q}^{(2)}\right]^3(38.2478 - 261.153\eta_\mathrm{Q}^2 + 79.2827\eta_\mathrm{Q}^4 - 2.27972\eta_\mathrm{Q}^6) \qquad (43\mathrm{b})$$

Surprisingly, both the second and third DOR moments are independent of the relative rotor phase, γ_r. This means that there are no possible combinations of spectra aquired with different relative rotor phases that can cancel all of the spinning sidebands without canceling the entire signal.

Bessel analysis of DAS and DOR sidebands

The moment analysis may have severe problems in practical cases since, in principle, an infinite number of sidebands must be taken into account, or else the short-time behavior of the rotational spin echoes must be analyzed very accurately. Therefore, the accuracy of the quadrupolar parameters is strongly dependent on the signal-to-noise ratio of the spectra. Furthermore, this method will fail if two or more peaks in a spectrum overlap. A solution to these problems is provided by the analysis of MAS sideband

TABLE 5

Coefficients of second moment, $M_2 = \sum_{m=0}^{4} [\delta^4(3+\eta^2)^2/35]c_m \cos(m\phi)$, of DAS spectrum

k_t	c_0	c_1	c_2	c_3	c_4
1.0	0.575305	0.0231429	0.0462857	−0.00880272	0.0143401
2.0	0.67649	0.00752257	0.0394718	0.0346066	−0.00557871
3.0	0.76751	0.00218131	0.0181915	0.0294343	−0.0172256
4.0	0.833515	0.000386193	0.00533654	0.0151341	−0.0174731
5.0	0.881699	0.00000000	0.0000000	0.0000000	0.0000000

TABLE 6

Coefficients $c_{i,j}$ (k_t) in third moment of DAS spectrum

i	j	k_t				
		1 $\times 10^{-4}$	2 $\times 10^{-5}$	3 $\times 10^{-6}$	4 $\times 10^{-6}$	5 $\times 10^{-3}$
0	0	59.8784	1104.72	16381.9	20437.1	23.4809
	2	−617.817	−10246.6	−130835	−149443	−162.156
	4	170.558	2890.75	38175.6	44563.6	49.0797
	6	−6.14889	−99.2240	1210.76	−1340.36	−1.42215
1	0	48.7159	307.501	2238.31	1352.53	–
	2	378.641	3487.90	31491.6	22304.2	–
	4	−57.078	−604.255	5754.62	−4205.08	–
	6	5.87744	50.6531	444.052	308.756	–
2	0	42.2577	168.462	1005.12	442.213	–
	2	525.393	164.81	−3089.92	−2372.00	–
	4	−93.2775	56.9653	1245.05	772.785	–
	6	7.52973	6.19424	13.3293	−18.3651	–
3	0	12.9165	55.0751	253.827	74.4609	–
	2	−293.504	−1251.48	−5767.74	−1691.99	–
	4	72.399	308.704	1422.74	417.364	–
	6	−3.30458	−14.0905	−64.9394	−19.0502	–
4	0	6.45826	10.4963	30.4359	5.38857	–
	2	−146.752	−238.509	−691.600	−122.445	–
	4	36.1995	58.8332	170.598	30.2037	–
	6	1.65229	2.68538	7.78677	−1.37862	–

intensities developed by Herzfield and Berger, using Bessel functions [13].

From the properties of Bessel functions $\{J_k(z)\}$, we can derive

$$\exp(-iz\ \mathrm{e}^{-i\theta}) = \sum_{k} \mathscr{J}_k(z)\ \mathrm{e}^{-ik\theta} \qquad (44)$$

where

$$\mathscr{J}_k(z) = \sum_{k'} (-i)^{k'} J_{k'}(z) J_{k-k'}(-iz) \qquad (45)$$

and where z is a complex number. The inverse transformation of eqn. (44) is

$$\mathscr{J}_k(z) = \frac{1}{2\pi} \int_0^{2\pi} \exp\left[i(k\theta - z\ \mathrm{e}^{-i\theta})\right]\, \mathrm{d}\theta \qquad (46)$$

TABLE 7

Coefficients $s_i(k_t) \left(\frac{-i3\times 10^{-5}}{7}\right) \delta_Q^4\ (3+\eta_Q^2)^2$ of third moment of DAS spectrum

k_t	s_1	s_2	s_3	s_4
1.0	0	0	0	0
2.0	−9.29785	115.355	197.359	50.1505
3.0	−43.0639	147.172	136.436	21.8131
4.0	−52.4194	90.8046	48.0288	4.63432
5.0	0	0	0	0

DAS sidebands

Using eqn. (44) and the total evolved phase of the magnetization under DAS given in eqn. (25), the fid can be expanded into a Bessel function series as

$$g_{\mathrm{DAS}}(t)=\left\{\prod_{m\neq 0}\sum_{i_m,j_m,k_m,l_m}\mathscr{J}_{i_m}\left[B_m^{\mathrm{DAS}}(\theta_2)\right]\right.$$
$$\times\mathscr{J}_{j_m}\left[-B_m^{\mathrm{DAS}}(\theta_2)\right]\mathscr{J}_{k_m}\left[B_m^{\mathrm{DAS}}(\theta_1)\right]$$
$$\left.\times\mathscr{J}_{l_m}\left[-B_m^{\mathrm{DAS}}(\theta_1)\right]\right\}$$
$$\times\exp\left\{-i\left[N_\alpha\alpha+N_\phi\phi\right.\right.$$
$$\left.\left.+\left(N_{\mathrm{r}_1}+N_\phi\right)\omega_{\mathrm{r}_1}t+N_{\mathrm{r}2}\omega_{\mathrm{r}_2}t\right]\right\}\qquad(47)$$

where

$$N_\alpha=\sum_{m=-4}^{4}m(i_m+j_m+k_m+l_m)\qquad(48a)$$

$$N_\phi=\sum_{m=-4}^{4}m(i_m+j_m)\qquad(48b)$$

$$N_{\mathrm{r}_1}=\sum_{m=-4}^{4}mk_m\qquad(48c)$$

$$N_{\mathrm{r}_2}=\sum_{m=-4}^{4}mi_m\qquad(48d)$$

$$\omega_{\mathrm{r}_1}=\frac{1}{1+k_t}\omega_{\mathrm{r}}\qquad(48e)$$

$$\omega_{\mathrm{r}_2}=\frac{k_t}{1+k_t}\omega_{\mathrm{r}}\qquad(48f)$$

For a powder sample, we assume that all nuclear spins have an equal probability of being in any orientation. The fid of the powder sample is then given by integrating eqn. (47) over all Euler angles. After averaging eqn. (47) over α, the fid becomes

$$\overline{g_{\mathrm{DAS}}(t)}=\sum_{N_\phi}g_{N_\phi}(\theta_1,t)\,g_{-N_\phi}(\theta_2,t)\,\mathrm{e}^{-iN_\phi\phi}\qquad(49)$$

where

$$g_{N_\phi}(\theta,t)=\prod_{m\neq 0}\sum_{i_m}\sum_{j_m}\mathscr{J}_{i_m}[B_m(\theta)]$$
$$\times\mathscr{J}_{j_m}[-B_m(\theta)]\,\mathrm{e}^{-iN_{\mathrm{r}\omega\mathrm{r}t}}\qquad(50)$$

and

$$N_{\mathrm{r}}\omega_{\mathrm{r}}=\begin{cases}N_{\mathrm{r}_1}\omega_{\mathrm{r}_1} & \text{for } \theta=\theta_1\\ N_\phi\omega_{\mathrm{r}_1}+N_{\mathrm{r}_2}\omega_{\mathrm{r}_2} & \text{for } \theta=\theta_2\end{cases}\qquad(51)$$

The fid after averaging over α is thus a sum over N_ϕ of the products of the fid's $g(\theta_1)$ and $g(\theta_2)$, which arise from spinning at θ_1 and θ_2, respectively, and a phase factor $\mathrm{e}^{-iN_\phi\phi}$. The overall sideband pattern under DAS is a sum of convolution spectra involving two individual sets of sidebands due to the evolution during times t_1 and t_2. The summation disappears once averaging over the relative rotor phase is performed, and the sideband spectrum becomes simply a convolution of sideband patterns at θ_1 and θ_2.

In order to evaluate the sideband intensities, we have to apply to eqn. (49) the inverse transformation of the Bessel function given in eqn. (46). The resulting expression for the fid is

$$\overline{g_{\mathrm{DAS}}(t)}=\sum_{N_\phi}\sum_{N_1,N_2}I_{N_1}^*(\theta_1)$$
$$\times I_{N_1-N_\phi}(\theta_1)I_{N_2}(\theta_2)I_{N_2-N_\phi}^*(\theta_2)$$
$$\times\mathrm{e}^{-i[N_\phi\phi+(N_1\omega_{\mathrm{r}_1}+N_2\omega_{\mathrm{r}_2})t]}\qquad(52)$$

where

$$I_N(\theta)=\frac{1}{2\pi}\int_0^{2\pi}\mathrm{d}\alpha$$
$$\times\exp\left[i\left(N\alpha-\sum_{m\neq 0}B_m(\theta)\,\mathrm{e}^{-im\alpha}\right)\right]\qquad(53)$$

After averaging eqn. (52) over the remaining two Euler angles, β and γ, the powder averaged fid is given by

$$G_{\mathrm{DAS}}(t)=\sum_{N_1,N_2}I_{N_1,N_2}^{\mathrm{DAS}}\,\mathrm{e}^{-i(N_1\omega_{\mathrm{r}_1}+N_2\omega_{\mathrm{r}_2})t}\qquad(54)$$

where

$$I_{N_1,N_2}^{\mathrm{DAS}}=\frac{1}{4\pi}\int_0^{2\pi}\int_0^{\pi}\sin\beta\,\mathrm{d}\beta\,\mathrm{d}\gamma\sum_{N_\phi}I_{N_1-N_\phi}(\theta_1)$$
$$\times I_{N_1}^*(\theta_1)I_{N_2}(\theta_2)I_{N_2-N_\phi}^*(\theta_2)\,\mathrm{e}^{-iN_\phi\phi}\qquad(55)$$

As can be seen from eqn. (52), after $g_{N\phi}(\theta,t)$ is expanded into a Fourier series, the coefficients (sideband intensities) of each individual harmonic are dependent on the relative rotor phase between θ_1 and θ_2. This dependence might prove interesting for sideband suppression if the intensities varied symmetrically with the relative rotor phase. However, the dependence appears as an averaged form of multi-order trigonometric functions in eqn. (55). Because the order, N_ϕ, is determined by the ratio of the quadrupolar parameters and the spinning speed, the variation of the sideband intensities with the rotor phase changes as the sample spinning speed changes, and does not show any symmetry properties. This characteristic can also be seen in eqn. (26), where the symmetry of the coefficients B_m is dependent on the symmetry of A_m, unlike the case of DOR in which $A_{l,m}$ is truncated by the spinning of the inner rotor. Thus the evolved phase of the magnetization given by eqn. (25) does not have symmetry with respect to the relative rotor phase. Further proof of this property will be seen in the numerically simulated spectra.

The structure of the sidebands in DAS NMR spectra can be interpreted as follows. If we assume that $k_t = k_1/k_2$, where k_1 and k_2 are two integers, the maximum number of sidebands is $k_1 + k_2$ in one rotor cycle ω_r. Of course the intensities of the sidebands are different. In general those corresponding to small N_1 and N_2 in eqn. (52) have larger intensities, and, therefore, there are three main sidebands in one cycle whose frequencies are ω_{r_1}, ω_{r_2}, and ω_r, respectively. In the case where $k_t = 1$, two sidebands in the middle will overlap so that the whole pattern is uniquely determined by the frequency $\omega_r/2$. If $k_t = 5$, then the ω_{r_1} sidebands disappear and the difference between two sidebands is uniquely determined by $\omega_{r_2} = \frac{5}{6}\omega_r$. This condition leads to maximum effective rotational speed because the rotation at $\theta_1 = 0°$ commutes with the spin Hamiltonian.

Experimentally, if the rotor is not synchronized during spinning, the relative phase is a random variable for different acquisitions. This is equivalent to taking an average over the relative initial phase [$N_\phi = 0$ in eqn. (55)] and the sideband intensity becomes

$$\overline{I_{N_1,N_2}^{\mathrm{DAS}}} = \tfrac{1}{4\pi}\int_0^{2\pi}\int_0^{\pi}\sin\beta\,\mathrm{d}\beta\,\mathrm{d}\gamma\,|\,I_{N_1}(\theta_1)\,|^2 \times|\,I_{N_2}(\theta_2)\,|^2 \qquad (56)$$

The sideband intensities therefore are always positive.

DOR sidebands

Applying eqn. (44), with the total evolved phase of the magnetization under DOR given in eqn. (29), we obtain the fid arising from the central quadrupolar transitions as

$$g_{\mathrm{DOR}}(t) = \left\{ \prod_{m_1,m_2=-4}^{4} \sum_{K^1_{m_1,m_2}} \sum_{K^2_{m_1,m_2}} \mathscr{J}_{K^1_{m_1,m_2}}\left(B^{\mathrm{DOR}}_{m_1,m_2}\right) \times \mathscr{J}_{K^2_{m1,m2}}\left(-B^{\mathrm{DOR}}_{m_1,m_2}\right)\right\} \times \exp\left\{-i\left[\left(N_{r_1}\omega_{r_1} + N_{r_2}\omega_{r_2}\right)t + \gamma_r\left(N^1_{r_1} + N^2_{r_1}\right) + \alpha\left(N^1_{r_2} + N^2_{r_2}\right)\right]\right\} \qquad (57)$$

where

$$N^i_{r_1} = \sum_{m_1,m_2} m_1 K^i_{m_1,m_2} \qquad (58a)$$

$$N^i_{r_2} = \sum_{m_1,m_2} m_2 K^i_{m_1,m_2} \qquad (58b)$$

for $i = 1,2$

Averaging the fid expressed in eqn. (57) over the three Euler angles and then applying the inverse transformation of Bessel functions given in eqn. (46) yields

$$G_{\mathrm{DOR}}(t) = \frac{1}{2\pi^2}\sum_{N_{r_1},N_{r_2}}\int_0^{\pi}\sin\beta\,\mathrm{d}\beta \times\int_0^{2\pi}\mathrm{d}\gamma\, I^{\mathrm{DOR}}_{N_{r_1},N_{r_2}} e^{-i(N_{r_1}\omega_{r_1}+N_{r_2}\omega_{r_2})t} \qquad (59)$$

where

$$I^{\mathrm{DOR}}_{N_{r_1},N_{r_2}} = F^{\mathrm{DOR}}_{N_{r_1},N_{r_2}} \sum_{N_r} F^{\mathrm{DOR}\,*}_{N_r,N_{r_2}}\ \mathrm{e}^{-i(N_{r_1}+N_r)\gamma_r} \qquad (60)$$

and

$$F^{\mathrm{DOR}}_{N_{\mathrm{r}_1},N_{\mathrm{r}_2}} = \frac{1}{(2\pi)^2}\int_0^{2\pi}\mathrm{d}\theta_1\int_0^{2\pi}\mathrm{d}\theta_2 \times \exp\left\{-i\left[N_{\mathrm{r}_1}\theta_1 + N_{\mathrm{r}_2}\theta_2 + \sum_{m_1,m_2=-4}^{4} B^{\mathrm{DOR}}_{m_1,m_2}\,\mathrm{e}^{-i(m_1\theta_1+m_2\theta_2)}\right]\right\} \tag{61}$$

In the limit that the inner rotor spins infinitely fast, the coefficients B_{m_1,m_2} given in eqn. (31) are equal to zero for all m_2 except $m_2 = 0$. This property leads to the fact that the integration of eqn. (61) over θ_2 is equal zero except for $N_{\mathrm{r}_2} = 0$, and that the number of integrations required to determine F reduces to one.

From Eqns. (60) and (61), it can be seen that both the phases and intensities of the sidebands are dependent on the relative rotor phase between two applied rotations. Such a property is different from MAS where all sidebands are in phase after averaging over the Euler angle α. It is therefore interesting to find out if there is symmetry in the variation of the sideband intensities and their phases with respect to the relative rotor phase. In order to derive this symmetry for DOR sidebands, we extend to the limiting case in which the spinning speed of the inner rotor is much larger than the second-order quadrupolar interaction. Hence all terms containing ω_{r_2} in eqn. (31) can be ignored, yielding the phase of the magnetization evolved at time t as

$$\varphi^{\mathrm{DOR}}(t) = \sum_{m=1}^{4} B^{\mathrm{DOR}}_{m0}\left[\sin m(\gamma_{\mathrm{r}} + \omega_{\mathrm{r}_1}t) - \sin m\gamma_{\mathrm{r}}\right] \tag{62}$$

Now we can define $\varphi^{\mathrm{DOR}}_{\mathrm{e}}$ and $\varphi^{\mathrm{DOR}}_{\mathrm{o}}$ by

$$\varphi^{\mathrm{DOR}}_{\mathrm{e}}(t,\gamma_{\mathrm{r}}) = \sum_{m=2,4} B^{\mathrm{DOR}}_{m0}\left[\sin m(\gamma_{\mathrm{r}} + \omega_{\mathrm{r}_1}t) - \sin m\gamma_{\mathrm{r}}\right] \tag{63a}$$

$$\varphi^{\mathrm{DOR}}_{\mathrm{o}}(t,\gamma_{\mathrm{r}}) = \sum_{m=1,3} B^{\mathrm{DOR}}_{m0}\left[\sin m(\gamma_{\mathrm{r}} + \omega_{\mathrm{r}_1}t) - \sin m\gamma_{\mathrm{r}}\right] \tag{63b}$$

and, substituting $\gamma_{\mathrm{r}} = 0°$ and $\gamma_{\mathrm{r}} = 180°$ into eqn. (63), represent the total evolved phase of the magnetization as

$$\varphi^{\mathrm{DOR}}(t,\gamma_{\mathrm{r}} = 0°) = \varphi^{\mathrm{DOR}}_{\mathrm{e}}(t,\gamma_{\mathrm{r}} = 0°) + \varphi^{\mathrm{DOR}}_{0}(t,\gamma_{\mathrm{r}} = 0°) \tag{64a}$$

$$\varphi^{\mathrm{DOR}}(t,\gamma_{\mathrm{r}} = 180°) = \varphi^{\mathrm{DOR}}_{\mathrm{e}}(t,\gamma_{\mathrm{r}} = 0°) - \varphi^{\mathrm{DOR}}_{\mathrm{o}}(t,\gamma_{\mathrm{r}} = 0°) \tag{64b}$$

If we average the fid generated by eqn. (64), the total fid signal for central transition is

$$\overline{G_{\mathrm{DOR}}(t)} = \int_{\Omega}\mathrm{d}\Omega\;\mathrm{e}^{-i\varphi^{\mathrm{DOR}}_{\mathrm{e}}(t,\gamma_{\mathrm{r}}=0°)} \times\left\{\mathrm{e}^{-i\varphi^{\mathrm{DOR}}_{\mathrm{o}}(t,\gamma_{\mathrm{r}}=0°)} + \mathrm{e}^{i\varphi^{\mathrm{DOR}}_{\mathrm{o}}(t,\gamma_{\mathrm{r}}=0°)}\right\} \tag{65}$$

Using eqn. (44), the fid can be written as a series of Bessel functions as

$$\overline{G_{\mathrm{DOR}}(t)} = \int_{\Omega}\mathrm{d}\Omega\;\mathrm{e}^{-i\varphi^{\mathrm{DOR}}_{\mathrm{e}}(t,\gamma_{\mathrm{r}}=0°)}\sum_{N,k}\left[1 + (-1)^N\right] \times J_{N-3k}\left(B^{\mathrm{DOR}}_{10}\right)J_k\left(B^{\mathrm{DOR}}_{30}\right)\mathrm{e}^{iN\omega_{\mathrm{r}_1}t} \tag{66}$$

In eqn. (66), $\varphi^{\mathrm{DOR}}_{\mathrm{e}}$ only contributes to even sidebands because the basic harmonic frequency is $2\omega_{\mathrm{r}_1}$. The odd sidebands are then determined by the second part. When N is an odd number, the intensities of all odd-order harmonics are zero. This reveals an inversion symmetry of the odd number sideband intensities at $\gamma_{\mathrm{r}} = 0°$ and $\gamma_{\mathrm{r}} = 180°$. Such a feature can be used to suppress odd number sidebands experimentally by adding two spectra obtained at $\gamma_{\mathrm{r}} = 0°$ and $\gamma_{\mathrm{r}} = 180°$.

The DOR sidebands will be in phase only after averaging eqn. (60) over the relative rotor phase. Experimentally this can be done by accumulating the fid without synchronizing the outer rotor. The fid under DOR then becomes

$$\overline{G_{\mathrm{DOR}}(t)} = \frac{1}{2\pi^2} \sum_{N_{r_1},N_{r_2}} \int_0^{\pi} \sin\beta \, d\beta \times \int_0^{2\pi} d\gamma \, | F^{\mathrm{DOR}}_{N_{r_1},N_{r_2}} |^2 \, e^{-i(N_{r_1}\omega_{r_1}+N_{r_2}\omega_{r_2})t} \tag{67}$$

Numerical calculations of the sideband intensities

DAS and DOR sideband intensities have been evaluated by numerical integration of eqns. (52), (56), (60) and (67) for a variety of cases. Composite ten-point Gaussian (Gauss–Legendre) quadrature has been used to approximate all

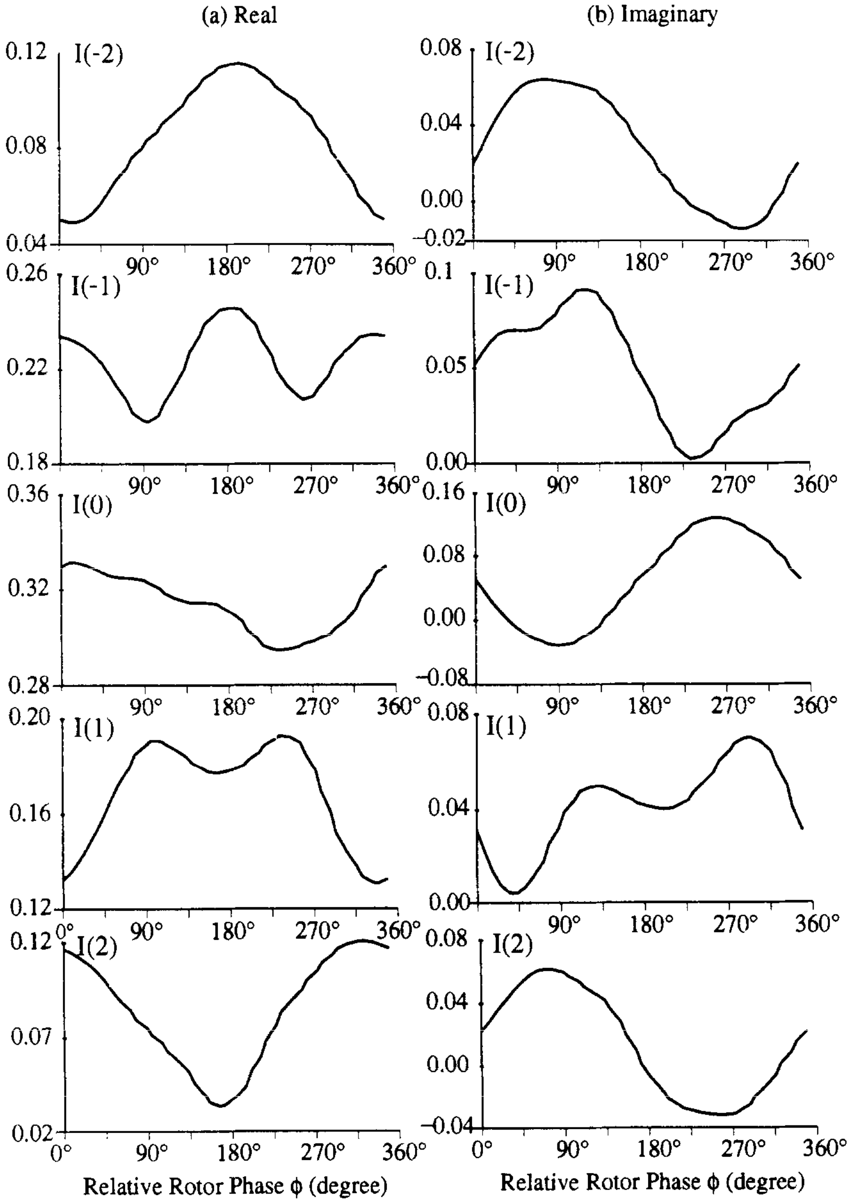

Fig. 10. Variation of simulated DAS sideband intensities, I_{N_1,N_2}, as the relative phase, ϕ, changes, for the case that $k_t = 1$, $\theta_1 = 37.38°$, and $\theta_2 = 79.19°$. The quadrupolar coupling constant is 405 kHz, and the asymmetry parameter is 0.72 (sodium oxalate). The sample spinning speed is 3 kHz, and the Larmor frequency is 105.8 MHz. Dashed lines correspond to negative N_1 values.

integrals over α, β, γ. Owing to a complicated orientation dependence, simulation of these sideband intensities is more time consuming than it is for MAS, especially in the case of DOR.

From eqn. (52), we see that the DAS sideband intensities and even their phases depend on the relative phase ϕ. As has been discussed, this dependence does not exhibit any symmetry which can be used to suppress DAS sidebands. This conclusion can be further proven by examining the variation of the DAS sideband intensities as the relative rotor phase, ϕ, changes from 0° to 360°, which is shown in Fig. 10. In this figure the real components of the DAS sidebands are always positive for $k_t = 1$, corresponding to $\theta_1 = 37.38°$ and $\theta_2 = 79.19°$. The spinning speed is $\omega_r = 2$ kHz or higher, and we assume that the quadrupolar coupling constant ω_Q is 405 kHz, the asymmetry parameter η_Q is 0.72, and the Larmor frequency is 105.8 MHz.

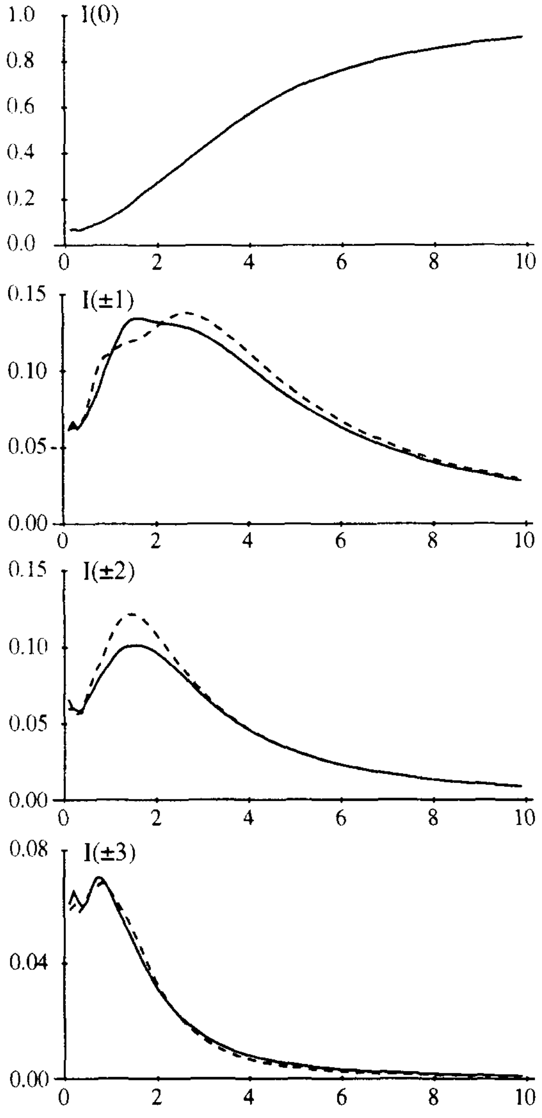

Fig. 11. Variation of simulated DAS sideband intensities, I_{N_1,N_2} with the sample spinning speed for the case that $k_t = 1$, corresponding to $\theta_1 = 37.38°$ and $\theta_2 = 79.19°$, and $N_2 = 0$, $N_1 = 0$, ± 1, ± 2. The quadrupolar coupling constant of the sodium-23 nucleus is 405 kHz, its asymmetry parameter is 0.72, and the Larmor frequency is 105.8 MHz. Dashed lines correspond to negative N_1 values.

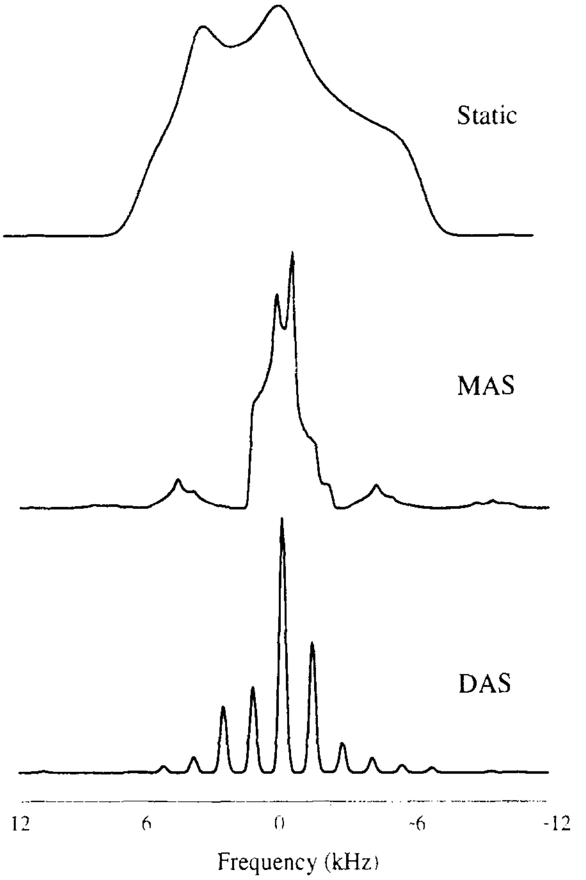

Fig. 12. Simulated DAS spectra using the same parameters as for sodium oxalate ($\omega_Q = 405$ kHz, $\eta_Q = 0.72$, $\omega_0 = 105.8$ MHz). (a) Static powder lineshape; (b) residual lineshape after MAS; (c) DAS spectrum obtained with $\omega_r = 3.36$ kHz.

Using eqn. (56), we have evaluated how the DAS sideband intensities vary with the spinning speed, ω_r, as shown in Fig. 11. As can be seen from this figure, the sideband intensities around the centerband are distributed more symmetrically than those in MAS. This feature makes the sideband intensities less sensitive to the asymmetry parameter compared to MAS.

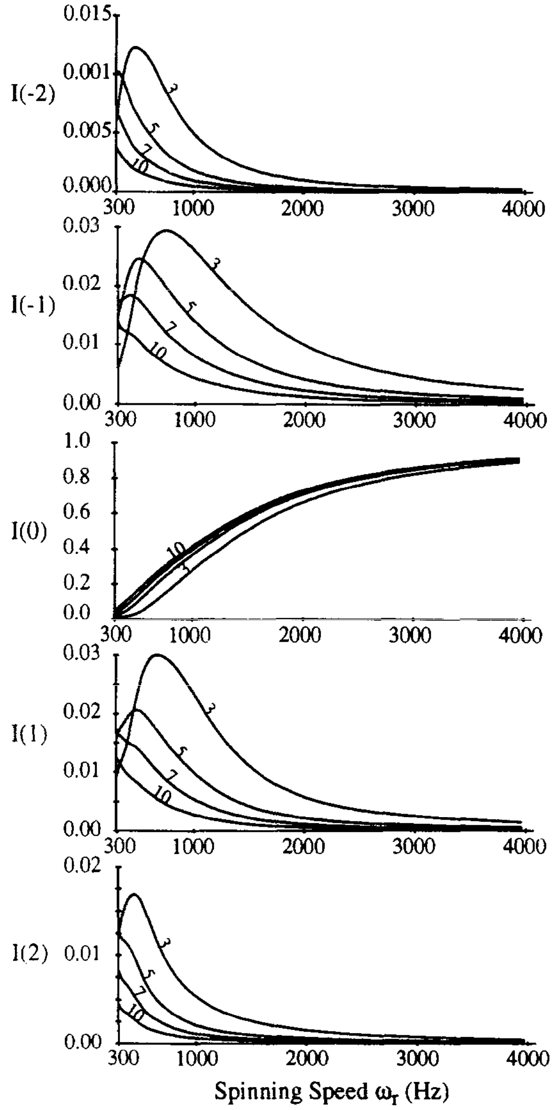

Fig. 13. Schematic variation of simulated sideband intensities as the spinning speed of the outer rotor, ω_{r_1}, changes, for different ratio between the two spinning speeds of the inner and the outer rotors, $\omega_{r_2}/\omega_{r_1}$, after average over the relative phase γ_r. $\omega_Q = 405$ kHz, $\eta_Q = 0.72$, and $\omega_0 = 105.8$ MHz (sodium oxalate).

Figure 12a shows the simulated spectra of polycrystalline sodium oxalate using the same parameters as in Fig. 11. The other simplest solution is for $k_t = 5$. In this case one of the rotation axes is aligned with the external magnetic field H_0 ($\theta_1 = 0$), and accordingly $B_m(0) = 0$ for all $m \neq 0$. Furthermore, in eqn. (56) the number of summations reduces to one. The frequency difference between two nearest sidebands is ω_{r_2}. Maximum spectral resolution can be obtained under these conditions.

Figure 13 shows how the DOR sideband intensities vary with the spinning speed of the outer rotor, for different ratios of the two spinning speeds after averaging over the relative rotor phase, γ_r.

As has been discussed, both the DOR sideband intensities and phases depend on the phase between the outer rotor and inner rotor. Experimental results and simulations show that even when $\gamma_r = 0°$ there are still phase differences among the individual sidebands. Figure 14 shows the variation of the sideband intensities, I_{N_1,N_2} for $N_2 = 0$, and $N_1 = 0, \pm 1, \pm 2$ with the relative phase. Both the intensities and phases of all of the sidebands vary with γ_r. The intensities of the real components of the even-order sidebands ($N_1 = 0, \pm 2$, *etc.*) are always positive, while the odd-order sidebands oscillate about zero. Especially interesting are the intensities of the odd-order sidebands, which at $\gamma_r = 0°$ are just the opposite of those at $\gamma_r = 180°$. The exact variation of the sideband intensities with the relative rotor phase is determined by the quadrupolar parameters, ω_Q and η_Q, as well as the two spinning speeds of the inner and outer rotors. In practice, these variations can be used to extract the quadrupolar information by comparing simulated and experimental results. As an example, Fig. 15 shows sideband intensities obtained expeimentally from sodium oxalate under DOR by varying the relative phase. These values are in agreement with the simulated results shown in Fig. 14. In actuality, the extraction of the quadrupolar parameters can be achieved by fitting only the variation of the centerband ($N_{1,2} = 0$) intensities with respect to the relative rotor phase. The advantage of this method is that the centerband is usually the most

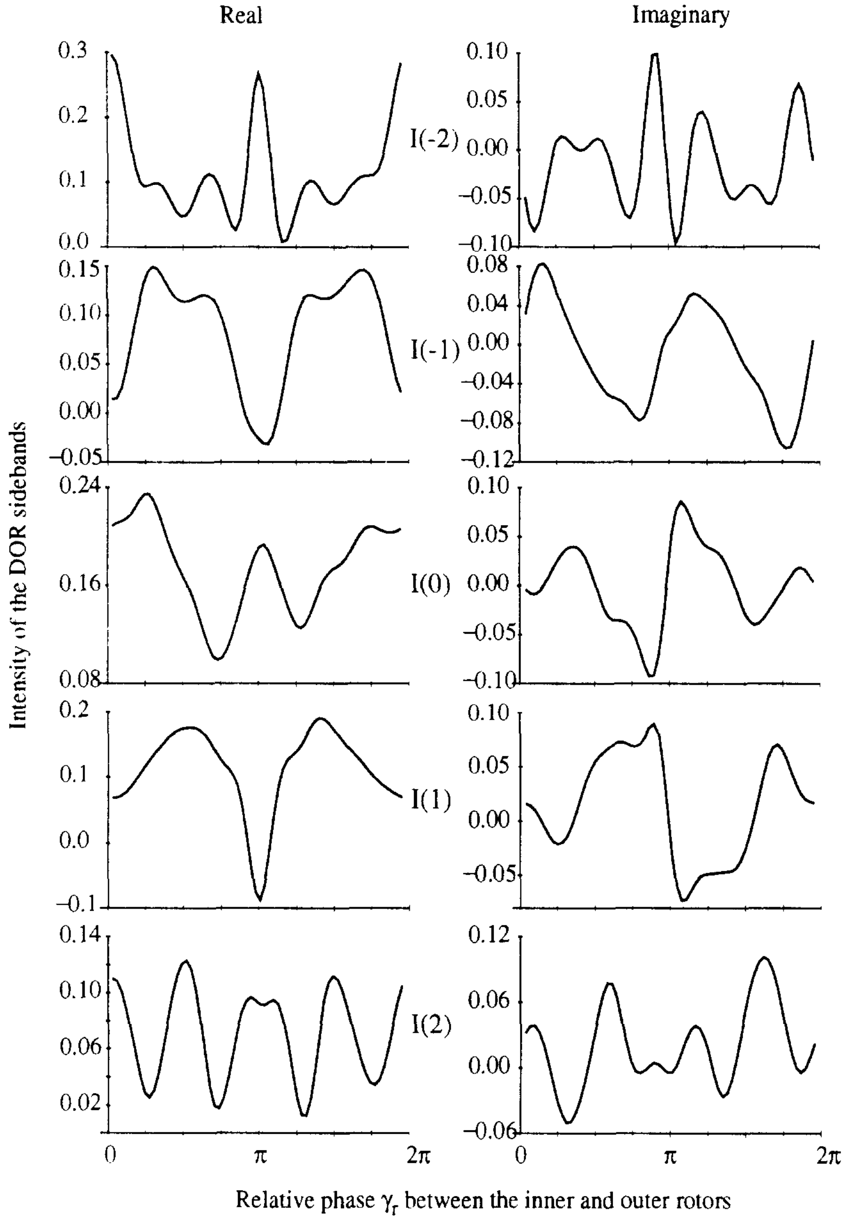

Fig. 14. Variations of the simulated DOR sideband intensities with different relative rotor phases γ_r between the inner and outer rotors. Parameters are $\omega_Q = 405$ kHz, $\eta_Q = 0.72$, and $\omega_0 = 105.8$ MHz. The outer rotor spinning speed is 700 Hz while the inner rotor sinning speed is 3.3 kHz.

intense peak in the sideband envelope which allows us to obtain the best accuracy when fitting experimental results with simulations. Figure 16 contains parametric plots showing how the centerband intensity varies with γ_r.

We have shown above that DOR exhibit inversion symmetry at $\gamma_r = 0°$ and $\gamma_r = 180°$ under the limiting condition of fast inner spinning speed. This property holds true even under slow inner spinning speeds for sidebands near the center-

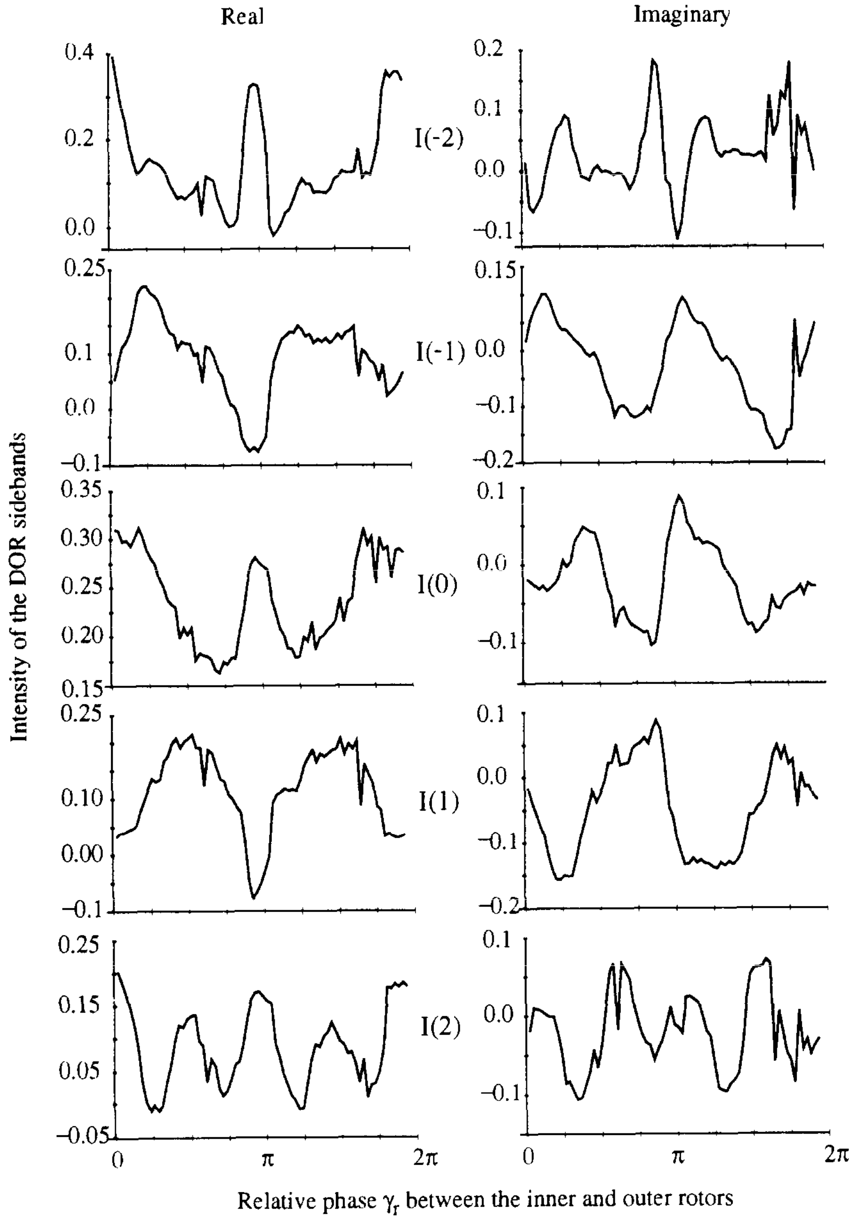

Fig. 15. Experimental DOR sideband intensities in sodium oxalate as the relative rotor phase γ_r between the inner and outer rotors changes. $\omega_Q = 405$ kHz, $\eta_Q = 0.72$, and $\omega_0 = 105.8$ MHz. The outer rotor spinning speed is 700 Hz while the inner rotor rotates at the rate of 3.3 kHz.

band. Practically, such an inversion symmetry can be used to eliminate the odd sidebands and thereby improve the spectral resolution. To achieve this, the outer rotor has to be synchronized at $\gamma_r = 0°$ and $\gamma_r = 180°$. After adding two spectra together, the odd sidebands near the centerband can be totally suppressed [11,30]. Figure 17 shows experimental and simulated results for sodium oxalate.

Conclusion

We have described general theories of DAS and DOR sidebands based on moment and Bessel function analysis. From the moment analysis we have shown that the third and higher moments increase with ω_r, and that the envelope of the DAS and DOR sidebands changes as a quasi-super-Lorentzian lineshape with increasing spinning speed. Bessel function analysis has been used to evaluate the structure and intensity of the DAS and DOR sidebands, and the dependence of the sideband intensities on the quadrupolar parameters and the spinning speeds has been numerically simulated. All the results are in agreement with the experiments. In DAS spectra,

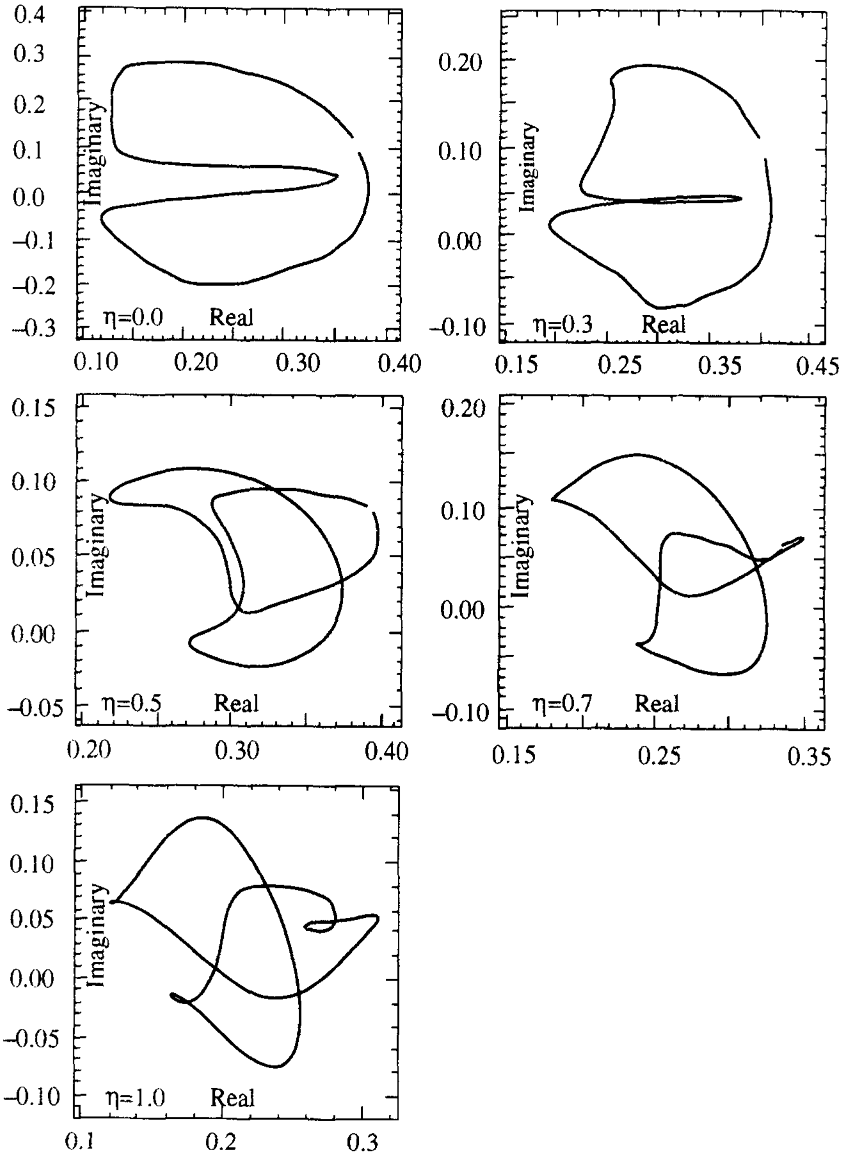

Fig. 16. Parametric plots showing the variation of the DOR centerband intensities as the relative rotor phase (γ_r) between the inner and outer rotors changes from 0° to 360°. Results for different asymmetry parameters are shown. $\omega_Q = 433$ kHz, and $\omega_0 = 105.8$ MHz. The outer rotor spinning speed is 700 Hz while the inner rotor spins at the rate of 3.3 kHz.

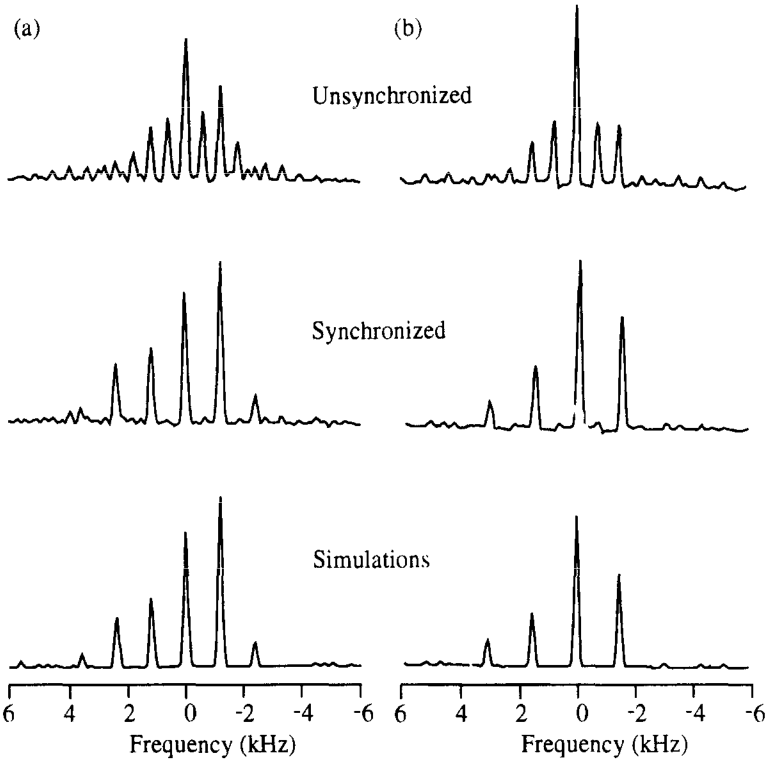

Fig. 17. Suppression of odd number sidebands by use of the inversion symmetry about the relative phase $\gamma_r = 0$ and $\gamma_r = \pi$. The outer rotor spins (a) at 604 Hz, and (b) at 800 Hz. A computer simulation is shown in the bottom row, with parameters $\omega_Q = 405$ kHz, $\eta_Q = 0.72$, and $\omega_0 = 105.8$.

the sidebands consist of a sum of convolutions involving two individual sets of sidebands generated during the evolution times of t_1 and t_2, respectively, over the relative rotor phase ϕ. Both the intensities and the phases of the sidebands vary with the relative rotor phase, but no inversion symmetry similar to that in DOR has been found. After averaging over the relative phase, the sideband intensities become more or less symmetric around the centerband, especially when the spinning is fast, and thus they are not very sensitive to the asymmetry parameter. The dependence on the time ratio between the two evolution periods in the DAS experiment results in a complicated sideband structure. New sidebands appear over one rotational cycle, adding $k_1 + k_2$ signals when the time ratio is $k_t = k_1/k_2$. For example, in the case of $k_t = 1$ ($k_1 = k_2 = 1$), there are three sidebands: two are at $\omega_r/2$ and the other is at ω_r, where ω_r is the sample spinning speed. We have also discussed the possibility of extracting the quadrupolar parameters by simulating the sideband intensities.

In DOR spectra, the sidebands are highly resolved only if the ratio of the two spinning speeds is larger than 4. The sideband intensities and phases are determined by the spinning speeds, the quadrupolar parameters, and the relative rotor phase between the outer and inner rotors. The odd numbered sideband intensities near the centerband exhibit an inversion symmetry at $\gamma_r = 0$ and $\gamma_r = \pi$. This symmetry property which has been proven theoretically in the limiting case where the inner spinning speed is much larger than the second-order quadrupolar coupling constant, permits complete suppression of the odd numbered sidebands.

The DOR centerband intensities are sensitive to the relative rotor phase. By simulating this dependence we may accurately extract the quadrupolar parameters.

The above results can be applied to any other inhomogeneous interaction. For homogeneous interactions, if ω_{r_2} in DOR is much larger than the amplitude of the interaction, we can average over the second rotation first, which reorients the spins along the rotation axis. The broadening then becomes approximately inhomogeneous. By applying the first rotation without the condition of fast spinning, the broadened line will split into a set of sidebands and the spectral resolution will be much higher than that resulting from MAS with the same spinning speed as the outer rotor.

Acknowledgement

This work was supported by the Director, Office of Energy Research, Office of Basic Energy Sciences, Materials Sciences Division of the U.S. Department of Energy, under Contract no. DE-AC03-76SF00098. J.H.B. acknowledges support from the N.S.F.

References

1 E. Kundla, A. Samoson and E. Lippmaa, *Chem. Phys. Lett.*, 83 (1981) 229.

2 A. Samoson, E. Kundla and E. Lippmaa, *J. Magn. Reson.*, 49 (1982) 350.

3 S. Ganapathy, S. Schramm and E. Oldfield, *J. Chem. Phys.*, 77 (1982) 4360.

4 E.R. Andrew, A. Bradbury and R.G. Eades, *Nature (London)*, 182 (1958) 1659.

5 I.J. Lowe, *Phys. Rev. Lett.*, 2 (1959) 285.

6 A. Samoson, B.Q. Sun and A. Pines, in D.M.S. Bagguley (Ed.), *Pulsed Magnetic Resonance: NMR, ESR, and Optics (A Recognition of E.L. Hahn)* Clarendon, Oxford, 1992.

7 K.T. Mueller, B.Q. Sun, G.C. Chingas, J.W. Zwanziger, T. Terao and A. Pines *J. Magn. Reson.*, 86 (1990) 470.

8 A. Llor and J. Virlet, *Chem. Phys. Lett.*, 152 (1988) 248.

9 A. Samoson, E. Lippmaa and A. Pines, *Mol. Phys.*, 65 (1988) 1013.

10 B.F. Chmelka, K.T. Mueller, A. Pines, J. Stebbins, Y. Wu and J.W. Zwanziger, *Nature (London)*, 339 (1989) 42.

11 Y. Wu, B.Q. Sun, A. Pines, A. Samoson and E. Lippmaa, *J. Magn. Reson.*, 89 (1990) 296.

12 M.M. Maricq and J.S. Waugh, *J. Chem. Phys.*, 70 (1979) 3300.

13 J. Herzfeld and A.E. Berger, *J. Chem. Phys.*, 73 (1980) 6012.

14 B.Q. Sun and A. Pines, to be published.

15 M. Mehring, *Principles of High Resolution NMR in Solids*, 2nd edn., Springer-Verlag, Berlin, 1983.

16 U. Haeberlen and J.S. Waugh, *Phys. Rev.*, 175 (1968) 453.

17 U. Haeberlen, *High Resolution NMR in Solids: Selective Averaging*, Academic Press, New York, 1976.

18 D.L. VanderHart, *J. Chem. Phys.*, 84 (1985) 1196.

19 A. Messiah, *Quantum Mechanics*, North-Holland, Amsterdam, 1961.

20 L.L. Buishvili and M.G. Menabde, *Sov. Phys. JETP*, 50 (1979) 1176.

21 N.N. Bogolubov and Y.A. Mitropolsky, *Asymptotic Methods in the Theory of Non-linear Oscillations* Gordon and Breach, New York, 1961.

22 Z. Peng, B.Q. Sun and A. Pines, to be published.

23 M.E. Rose, *Elementary Theory of Angular Momentum*, Wiley, New York, 1957.

24 G.J. Bowden and W.D. Hutchison, *J. Magn. Reson.*, 67 (1986) 403.

25 K.T. Mueller, A. Pines and G. Chingas, *Rev. Sci. Instrum.*, 62 (1991) 1445.

26 P.J. Grandinetti, J.H. Bultisberger, A. Llor, Y.K. Lee, U. Werner and A. Pines, *J. Magn. Reson. A*, in press.

27 P.J. Grandinetti, Y.K. Lee, J.H. Baltisberger, B.Q. Sun and A. Pines, *J. Magn. Reson. A*, in press.

28 J.H Van Vleck, *Phys. Rev.*, 74 (1948) 1168.

29 A. Abragam, *Principles of Nuclear Magnetism*, Clarendon, Oxford, 1982.

30 A. Samoson and E. Lippmaa, *J. Magn. Reson.*, 84 (1989) 410.